This manuscript is a **preprint** and has been submitted for publication. This manuscript has undergone one round of peer review, but has not yet been formally accepted for publication. Subsequent versions of this manuscript may thus have different content. Please feel free to contact any of the authors directly or to comment on the manuscript. We welcome feedback!

# Mechanical Stratigraphy Controls Normal Fault Growth and Dimensions, Outer Kwanza Basin, Offshore Angola

**David Redpath[1*], Christopher A.-L Jackson[1], Rebecca E. Bell[1]**

Basins Research Group (BRG), Department of Earth Science & Engineering, Imperial College, Prince Consort Road, London, SW7 2BP, UK

*Corresponding author: David Redpath (david.redpath16@imperial.ac.uk)

**Key Points:**

- Mechanical stratigraphy and fault interactions control the extent to which faults adhere to displacement-length scaling relationships.
- Fault growth and displacement-length relationships must be considered in context of local factors to be adequately described and understood.
- Detailed kinematic analysis on faults developing within the same overall tectono-stratigraphic setting can shed light on the kinematics of fault growth.

## Abstract

Mechanical stratigraphy controls the growth patterns and dimensions of relatively small normal faults, yet how its influences the development of much larger structures remains unclear. Here we use 3D seismic reflection data from the Outer Kwanza Basin, offshore Angola to constrain the geometry and kinematics of several normal faults formed in a deep-water clastic succession. The faults are up to 6.3 km long, 1.9 km tall, and have up to 44 m of throw. Aspect ratios and lower-tip throw gradients are greater for faults that terminate downwards at a c. 100 m thick, mass-transport complex (MTC) (up to 5.2 and 0.12) than for those that offset it (up to 2.7 and 0.01). Faults that offset the MTC invariably have >30 m of throw. Based on their geometric properties and throw patterns, we interpret that the faults nucleated above the MTC and propagated down towards it. Upon encountering this unit, which we infer was weaker and behaved in a more ductile manner than encasing strata, tip propagation was halted until tip stresses were sufficiently high (corresponding to minimum throw of c. 30 m) to breach it. Faults with smaller throw were unable to breach the MTC. We argue that using only geometric criteria to determine fault growth patterns can mask the not insignificant control mechanical stratigraphy has on fault kinematics. Mechanical stratigraphy therefore has a key control on the growth of large, seismic-scale normal in a similar way to that observed for far smaller structures.



**Key Words:** Fault growth; Fault scaling; Fault geometry, Mechanical stratigraphy; Fault kinematics


## 1.0 Introduction

Understanding the geometry and growth of normal faults is crucial for a range of geoscience disciplines. For example, these structures control landscape evolution and sediment transport pathways in areas of continental extension (e.g. Gibbs, 1984, Leeder and Gawthorpe, 1987, McClay, 1990, Gawthorpe and Hurst, 1993, Trudgill and Cartwright, 1994, Peacock and Sanderson, 1994, Eliet and Gawthorpe, 1995, Gawthorpe and Leeder, 2000, Childs et al., 2003), the magnitude and recurrence interval of potentially hazardous earthquakes (e.g. Cowie and Scholz, 1992b, Walsh et al., 2002, Soliva et al., 2008, Wilkinson et al., 2015), and the occurrence and viability of hydrocarbon and geothermal resources (e.g. Bodvarsson et al., 1982, Fairley and Hinds, 2004, Rotevatn et al., 2007, Athmer and Luthi, 2011, Corbel et al., 2012, Serié et al., 2017).

Fault growth models were originally largely derived from global compilations of displacement (D) and length (L). More specifically, the recognition that D and L were positively correlated over several-orders-of-magnitude in the form $D = cL^n$, where $c$ is a constant and $n$ is between 1 and 1.5, led to the development of the so-called ‘propagating’ fault model, in which faults grow via a broadly synchronous increase in their displacement and length (e.g. Walsh and Watterson, 1988, Cartwright et al., 1995, Walsh et al., 2003, Nicol et al., 2005, Rotevatn et al., 2018, Nicol et al., 2020). More recent observations, primarily from 3D seismic reflection data imaging sedimentary basins, support an alternative model for normal fault growth, the so-called ‘constant-length” fault model. In this model, faults rapidly establish their near-final length *before* accumulating significant displacement (e.g. Walsh et al., 2002, Rotevatn et al., 2018). Rotevatn et al. (2018) also propose a hybrid growth model in which rapid fault lengthening by tip propagation and segment linkage (characteristics most consistent with the propagating fault model) principally occurs during the initial 20-30% of the faults lifespan (Stage 1), with this period followed by a second, more prolonged period of displacement accrual, during which time the fault does not significantly lengthen (characteristics more characteristic of the constant-length model) (Stage 2).

Fault geometry and growth can be controlled by the so-called ‘mechanical stratigraphy’ of the host rock. The term ‘mechanical stratigraphy’ encompasses: (i) the varying material properties of rock strata (e.g., measured properties such as compressive and tensile strengths, Young's modulus): (ii) the thicknesses of the mechanical layers, and (iii) the character and frictional properties of the transitions or boundaries between mechanical layers (e.g., sharp vs. gradational boundaries, and smooth vs. versus rugose contacts) (cf., Groshong, 2006, Ferrill and Morris, 2008, Laubach et al., 2009; Ferrill et al., 2017). In this context, ‘strong’, ‘stiff’, or ‘competent’ units (e.g., igneous rock, cemented sandstone or carbonate) tend to resist deformation, maintain bed length and thickness during deformation, accommodate little deformation before brittle failure or have low ductility, whereas ‘weak’, ‘soft’, or ‘incompetent’ strata (e.g., mudstone, salt) tend to deform relatively easily, change bed length and thickness during deformation, accommodate significant deformation before brittle failure or have high ductility (see Ferrill et al., 2017). Within this framework, the vertical and lateral propagation of faults that nucleate in ‘strong’ layers can be impeded vertically and laterally as they approach, deform, and mechanically interact with ‘weak’ layers, a situation common in heterogeneous sedimentary sequences. This behaviour can result in anomalous fault aspect ratios (i.e. the ratio between maximum fault height and length) and a deviation from the expected D-L relationship (Wilkins and Gross, 2002, Soliva et al., 2005a, Soliva and Benedicto, 2005). For example, a fault may preferentially propagate along-strike (i.e. laterally) in competent layers, thereby restricting its vertical height and increasing its aspect ratio, as well as restricting its ability to accumulate displacement; such faults may thus appear ‘under-displaced’. Short- and long-range stress interactions between salt bodies and faults (e.g. Tvedt et al., 2013), and between neighbouring faults (e.g. Peacock and Sanderson, 1991, Dawers and Anders, 1995, Martel, 1999, Peacock, 2002, Soliva et al., 2006), can also influence fault growth and geometry. To-date, however, most studies have focused on the control of mechanical stratigraphy on the geometry and growth of relatively small normal faults (i.e. displacements of <1 m and <100 m long; e.g., Wilkins and Gross, 2002, Soliva et al., 2005a, Soliva and Benedicto, 2005), and it is not clear if and how this control might scale with increasing mechanical unit thickness and fault size.

In this study, we use high-quality 3D seismic reflection data acquired by Compagnie Générale de Géophysique (CGG) from the Outer Kwanza Basin, offshore Angola to quantify the geometry of and displacement patterns on several normal faults (Fig. 1 and 2). These data allow us to assess how host rock mechanical properties, inferred from seismic facies analysis, influence fault growth and ultimate geometry, thereby allowing us to test fault growth models. These faults occur in a sedimentary basin where their host rock is dominated by slope mudstones, within which mechanical layering is imposed by a regionally developed mass-transport complex (MTC). We present marked differences in the geometry and kinematics of the faults, and explore the role of host rock heterogeneity and local mechanical interactions on their growth patterns. We show that the aspect ratios and displacement patterns vary on even closely spaced faults forming in the same host rock. We explore why faults can deviate from D-L scaling laws as they grow, even when they presently have D-L scaling relationships that broadly adhere to global compilations ($D = cL^n$; Fig. 2). Our study shows that D-L scaling (i.e. geometric) data alone does not allow us to determine the style of fault growth; detailed kinematic analysis using growth strata (e.g. Childs et al., 2003; Tvedt et al., 2013; Jackson & Rotevatn, 2013) and the analysis of faults of varying scales within a single population together provide more robust kinematic constraints.

## 2 Data and Methods

### *2.1 Data*

The study area is imaged by a high-quality, pre-stack, depth-migrated (PDSM) 3D survey with an aerial extent of 2915 km$^2$ (Fig. 1). The inline and crossline spacing for the survey is

25 m, with a vertical sampling interval of 2 m. The data are normal polarity (a peak indicates a downward increase in acoustic impedance) and zero phase, with a vertical resolution of c. 6 m at the seabed and c. 30 m at a depth of 3.5 km, approximated by a quarter of the dominant wavelength of the data (assuming average P-wave velocity of 2500 m/s) (see discussion by Evans and Jackson, 2019). In the absence of well-data, the lithology and absolute ages of the mapped seismic-stratigraphic units are constrained by using seismic facies analysis, seismic-stratigraphic principles, and by correlating their bounding horizons with three regionally mapped horizons (the Top Albian, Top Eocene and Top Miocene) presented by Hudec and Jackson (2004) (See also Spathopoulos, 1996, Marton et al., 2000, Hudec and Jackson, 2003, Hudec and Jackson, 2004, Jackson et al., 2005, Jackson and Hudec, 2008, Serié et al., 2017). The ages of other mapped horizons are inferred relative to these regional surfaces and documented geological events (e.g. periods of continental uplift and related salt tectonics). We use these age estimates to infer at which stratigraphic levels fault throw maxima occur, which may relate to the depth at which the faults nucleated (e.g. Hongxing and Anderson, 2007).

### *2.2 Seismic interpretation and fault characterisation*

We study a *c.* 70 km$^2$ area that is located between a c. 10 km elongate ridge of salt (i.e., salt wall) and a sub-circular dome of salt that has pierced the overlying strata (i.e., salt stock), the latter only being partially imaged along the western edge of the seismic survey (Fig. 1 and 3). Within this area we focus on sixteen, exceptionally well-imaged normal faults that form part of a larger array (Fig. 4 and 5). These faults are also selected because we can comprehensively map numerous (18) horizons in their flanking host rocks and, therefore, generate 3D throw strike-projections that allow us to constrain throw distributions across their surfaces (e.g. Walsh et al., 2003, Baudon and Cartwright, 2008, Duffy et al., 2015). We accurately mapped the faults on closely spaced (*c.* 50 m) seismic sections trending normal to fault strike. We therefore constrain their three-dimensional geometry, including their aspect ratio (i.e. length/down-dip height), with reasonable precision (Fig. 6) (Nicol et al., 1996, Polit et al., 2009). Where fault-related folding of the host rock is present adjacent to the fault surfaces, the cutoffs are extrapolated to remove the effects of this ductile or continuous deformation (e.g. Walsh and Watterson, 1987, Hongxing and Anderson, 2007, Jackson et al., 2017).

The shallow stratigraphy (*c.* 0-300 m below seabed) in the study area contains deep-water channels that incise up to 200 m into underlying stratigraphy (Fig. 7). This makes it difficult to confidently and regionally map near-seabed growth sequences that are now eroded (i.e. F6 and 7) (Fig. 7). Since many of the faults in the study area have shallow upper tips, where extensive channel-driven erosion occurs at the top of the fault (i.e. F3), it may be the case that aspect ratios become slightly higher than the original fault geometry (Fig. 6).

We follow the method of Walsh and Watterson (1991) to construct throw-distance (T-x) plots that show how throw varies along-strike on a given horizon, as well as strike-projections that show the throw distribution across the fault surface (e.g. Fig. 8) (Tvedt et al., 2013, Duffy et al., 2015, Collanega et al., 2018, Torabi et al., 2019). We also calculate throw gradients (i.e. change in throw/distance on fault surface over which the change occurs) across the fault surface, noting that relatively high gradients (> 0.15) may reflect retardation of fault tip propagation due to mechanical interactions with adjacent faults or host rock layers (e.g. Walsh and Watterson, 1988, Nicol et al., 1996). To determine where faults intersected the free surface during their growth, we calculate the expansion indices (EI) of packages of growth strata. EI is calculated by dividing the hanging-wall thickness of the package by its adjacent footwall thickness (e.g. Tvedt et al., 2013, Jackson et al., 2017). Finally, we define down-dip fault height (H) as the (sub)vertical distance from the fault upper to lower tip, and fault length (L) as the maximum (sub)horizontal distance between the fault's lateral tips (Fig. 6). Using these geometric data we determine fault aspect ratio (fault length/down-dip height of fault), which again can be used to infer whether the growth of a fault has been inhibited by mechanical interactions with adjacent faults or changes in host rock mechanical properties (Nicol et al., 1996, Soliva et al., 2005b).

## 3 Geological Setting

### *3.1 Outer Kwanza Basin*

The formation of the Inner and Outer Kwanza basins, offshore Angola initiated in the Early Cretaceous when rift pulses between the African and South American plates, and ultimately the breakup of Gondwana, resulted in the opening of the South Atlantic Ocean (Brice et al., 1982, Jackson et al., 2005, Hudec and Jackson, 2004; Serié et al., 2017) (Fig. 1).

During the Early Cretaceous, intermittent marine incursions resulted in restricted marine conditions and the deposition of thick, Aptian-Albian evaporites in the Inner and Outer Kwanza basins (e.g. Bate et al., 2001, Karner and Gambôa, 2007). Flow of this evaporite sequence from the Late Cretaceous until present controlled the overall, post-breakup structural evolution of the Kwanza Basins (Marton et al., 2000, Hudec and Jackson, 2004, Jackson and Hudec, 2008). For example, basinward tilting of the margin during the Late Cretaceous initiated the first post-salt phase of extension, causing the formation of predominantly seaward-dipping, salt-detached normal faults (Jackson et al., 2005). Post-salt deposition was initially dominated by relatively fine-grained deep-water sediments of the Iabe Group (Hudec and Jackson, 2003, Hudec and Jackson, 2004, Jackson and Hudec, 2008, Serié et al., 2017).

The second phase of significant post-salt extension occurred during the Neogene, triggered by onshore cratonic uplift (Jackson et al., 2005, Hudec and Jackson, 2004). Basementinvolved uplift of the continental shelf and upper slope in the Miocene resulted in an increase in the rate of seaward translation of the salt and its overburden, from *c*. 0.2 to 1 mm/yr (Jackson and Hudec, 2008, Jackson et al., 2005, Hudec and Jackson, 2004, Evans and Jackson, 2019). This resulted in a further 20 km of extension in the Outer Kwanza Basin (Hudec and Jackson, 2003, Jackson and Hudec, 2008, Evans and Jackson, 2019). Since the Miocene, sedimentation in the Outer Kwanza Basin has been dominated by hemipelagic clays and silts, with coarser-grained sediments being deposited in the basin in turbidite-fed channels and lobes (Serié et al., 2017, Howlett et al., 2020). Seismically chaotic, sharp-based, low-amplitude bodies of unknown composition are also observed in the post-Miocene sedimentary sequence; these are geophysically distinct from the fine- and coarse-grained slope deposits described above, which are typically characterised by moderate-to-high amplitude, continuous seismic reflections (Fig. 3) (see Serié et al., 2017, Howlett et al., 2020). Based on these seismic expression and the deep-water depositional setting, we suggest that these bodies represent mass-transport complexes (MTCs) (Moscardelli and Wood, 2008, Wu et al., 2019). We lack borehole data to constrain their lithology, but we tentatively suggest that they may be mudstone-dominated, based on the fact that the post-Miocene slope of Angola comprise very fine-grained rock types (e.g., Fraser et al., 2005).

## 4 Results

The normal fault array studied here sits within the axis of a N-trending minibasin (Fig. 3 and 4). The largest faults dip to the north and offset Cenozoic stratigraphy (Fig. 3 and 4). The D-L data for the faults broadly fit within the global D-L trend, sitting in the lower part of the dataset (Fig. 2). Within the fault array we can define three distinct fault groups based on their geometrical characteristics and inferred kinematic behaviour.

### *4.1 Planar faults (F1-F5)*

#### *4.1.1 Observations*

Planar faults are developed in the north of the study area, striking E-W and dipping 54-58° (Fig. 4 and 5). Striking orthogonal to the trend of adjacent salt wall, all of the faults dip northwards, with the exception of a single antithetic fault that dips southward (F1). The faults are 750–950 m tall and have maximum trace lengths of 1.8–4 km (Fig. 9). The maximum throw in this group is ~ 20 m, with the throw maxima occurring in Pliocene stratigraphy (Fig. 8 and 10). The upper tips of the planar faults are in Pliocene stratigraphy and their lower tips are located in Miocene stratigraphy (Fig. 5). F1 and F2 are quasi-elliptical, whereas F3 and F4 are elliptical (Fig. 8 b - e). The throw maxima for F1 and F2 are located near their centres, with throw ultimately decreasing towards their tips (Fig. 8 b and c). In contrast, throw maxima for F3 and F4 are slightly offset towards their lower halves (Fig. 8 d and e). This difference in the position of throw maxima is reflected in the lower-tip throw gradients. F1 and F2 show a relatively low throw gradient of 0.01, whereas F3 and F4 display throw gradients that are an order of magnitude greater (i.e. 0.12 and 0.11, respectively). The aspect ratio for planar faults with a throw maximum occurring along the Top Miocene horizon (i.e. F3 and F4) ranges from 3.5-5.2, whereas the ratio for those with a throw maximum in shallower, Pliocene stratigraphy is 2.7 (F1 and 2) (Figs 8 and 10). The lower tips of faults that exhibit relatively high aspect ratios (> 3.5), and which have maximum throws of < 20 m, are located at the top of a laterally extensive, seismically chaotic unit that we interpret as an MTC (F3 and F4; Fig. 11 a) (Moscardelli and Wood, 2008).

Only F1, which has the largest throw and shallowest upper tip of all the planar faults, is associated with growth strata. In this case, Pliocene growth strata have an EI of 1.2 (Fig. 10). Stratigraphic packages adjacent to all of the other faults in the planar fault group have EI <1.1

making it difficult to determine if these structures were ever growth faults that breached the free surface, or whether they grew as so-called 'blind' structures (e.g. Baudon and Cartwright, 2008, Jackson et al., 2017).

#### *4.1.2 Interpretation*

Their quasi-elliptical geometry, relatively low aspect ratio, and concentric throw distribution suggest F1 and F2 grew as mechanically unrestricted structures (cf. F3 and F4 below; see also Fig. 8) (Nicol et al., 1996). Figure 11a shows that the lower tips of F3 and F4 coincide with the MTC. Furthermore, these faults have aspect ratios greater than those of F1 and F2. Given that these relatively closely spaced faults formed in similar host rock in response to broadly similar driving stresses, one plausible interpretation for the greater aspect ratios of F3 and F4 is that their basal tips mechanically interacted with the MTC near the base of the faulted sequence. This could have resulted in their tips being pinned, inducing the preferential lengthening of these faults and thus giving rise to the development of relatively high aspect ratios (Fig. 9; 11a and 12). This interpretation is supported by the observation that the throw maxima for F3 and F4 are slightly offset towards their lower tips, and that lower-tip throw gradients are higher for these faults than F1 and F2 (Fig. 8d and e). These geometrical characteristics are consistent with enhanced strain accumulation in these areas as a function of vertical tip restriction during fault propagation (Fig. 8 and 12) (Wilkins and Gross, 2002).

### *4.2 Bifurcating faults (F6-F7)*

#### *4.2.1 Observations*

These faults are the longest in the studied array (> 5 km). They are characterised by a single fault segment at depth and two segments within shallower stratigraphy (F6 and F7; Fig. 4; 5 and 13). Bifurcating faults (F6 and F7) strike WNW-ESE and dip 54-60° northward (Fig. 4

and 5). The bifurcating faults contrast with the planar faults in two key ways; (i) they have larger throws (> 30 m; Fig. 11); and (ii) their basal tips lie beneath rather than above the MTC (Fig. 3 and 13).

F7 bifurcates upwards with a sub-horizontal, c. 1.2 km long branchline coinciding with the top of the MTC (Fig. 4; 5 and 13b). Maximum throw on F7 (c. 32 m) is also located near the top of the MTC and the throw gradient below the MTC is relatively low (0.08; Fig. 13b). The maximum down-dip height and trace length of F7 are 1.75 km and 6.4 km respectively, resulting in an aspect ratio of 3.6 (Fig. 9 and 13b).

At the structural level of the Pliocene, F6 consists of two parallel, overlapping fault segments separated by a narrow (~70 m) relay zone (Fig. 4 and 5). At depth these segments link and form a single fault surface (Fig. 4c; 5 and 13a). Similar to F7, the c. 1 km long, sub-horizontal branchline for the two upper segments of F6 coincides with the top of the MTC (Fig. 13a). In contrast to F7, the throw maximum for F6 occurs beneath (rather than above) the MTC, within Oligocene-Miocene stratigraphy (Fig. 13a). The distribution of throw on F6 defines a broad, U-shaped (depth) throw maximum that encircles the relay zone and its associated throw minimum, and which extends below the MTC and beneath the branchline (blue area; Fig. 13a). Relatively high throw gradients of up to c. 0.2 occur in the relay zone where the faults overlap (sharp transition from blue to white; Fig. 13a). F6 has a maximum down-dip height and length of 1.9 km and 6.3 km, respectively, resulting in an aspect ratio of 3.3.

*4.2.2 Interpretation*

The position of the maximum throw on F7 at the top of the MTC suggests the fault: (i) nucleated at this structural level; and/or (ii) nucleated elsewhere, possibly within the shallower stratigraphy, with the position of maximum throw migrating downwards with time.

Irrespective of where the fault nucleated, it was able to propagate through the MTC (Fig. 13b). This observation, coupled with the distinct decrease in throw and throw gradient immediately below the MTC, suggest that the MTC may have initially retarded downward or upward propagation of F7, causing strain to accumulate along the top of the MTC before the fault could propagate onward (Fig. 13b and 14a). We therefore suggest that in a similar way to F3 and F4, the tips of smaller, precursor segments were initially vertically restricted along the top of the MTC (Fig. 14a). However, unlike in the case of F3 and F4, the accumulation of additional displacement meant tip stresses around F7 became high enough to allow the fault to breach the MTC (Fig. 14a) (Wilkins and Gross, 2002).

In contrast to F7, we suggest F6 nucleated below (rather than above) the MTC based on the fact that maximum throw on the structure occurs at least partly below the MTC (Fig. 13a). Having nucleated below the MTC, F6 was then able to propagate upwards towards and ultimately through the MTC, locally bifurcating as it did (Fig. 14b). The throw distribution presently observed on F6 is consistent with numerically modelled throw distributions where a bifurcating planar frontal segment is present (Fig. 13a) (Soliva et al., 2008). We therefore suggest that the high throw values broadly encircling the relay zone, which is also associated with relatively high throw gradients (0.2), are as a result of tip interaction between the overlapping shallow segments during bifurcation and upward growth (Fig. 13a and 14b) (Nicol et al., 1996, Soliva et al., 2008, Nicol et al., 2017).

### *4.3 Arcuate faults (A1-A9)*

#### *4.3.1 Observations*

The group is characterised by faults defined by smooth, along-strike changes in their orientation, resulting in a bow-shaped, convex trace in map-view (Fig. 4). This group of faults are concentrated in the south of the study area, on the northern rim of a locally deep part of the minibasin on the west of the salt wall; this deep area is best-expressed at the Pliocene and Miocene structural level (Fig. 4a and b, respectively). Close to the salt wall these faults strike E-W, perpendicular to the salt-sediment interface, changing to a NE-SW strike ≥ 2 km away from the salt wall; this change in strike defines their plan-view geometry, with the faults following the overall shape of the deep part of the minibasin (Fig. 4a and b). Maximum throws on arcuate faults decrease with increasing distance from the salt wall; for example, A4 has a maximum throw of 44 m, whereas A9 has a maximum throw of ~10 m at 0.8 km and 3.5 km distance from the salt wall, respectively (Fig. 15a; see also Fig. 4a and b). We also note that arcuate faults appear overdisplaced, achieving similar maximum throws at only 60-70% of the strike length of other fault types (Fig. 15b). For example, A3 is 2.6 km long and has c. 35 m maximum throw, whereas F6 has comparable throw (c. 38 m) but is significantly longer (6.3 km) (Fig. 15b). Arcuate faults also have notably lower aspect ratios (i.e. 1.4-2.7) compared to the linked and planar faults (i.e. 2.7-5.2) (Fig. 9).

We can sub-divide the arcuate fault group based on the depth at which they occur, the detailed fault geometry, and the overall throw distribution. The first subgroup faults strike broadly E-W (i.e. similar to the overall trend of the fault array) and are present at greater depths (i.e. below -1900 m) than the second subgroup (A1-4; Fig. 4a - c). They exhibit down-dip heights of 1–1.9 km and maximum lengths of 1.5–4.7 km, yielding aspect ratios of 1.4 – 2.4 (Fig. 9). The largest faults in this subgroup, A3 and A4, have maximum throw values of 36 and 44 m, respectively, and offset the MTC, whereas those with throws < 30 m do not (Fig. 11b and c; and Fig. 15).

The second subgroup occurs at a shallower depth, in post-Miocene stratigraphy (A5-9; Fig. 3 and 4a). The upper tips of faults in this subgroup are located just 100 m beneath the seabed and they typically tip out ~150 m above the Top Miocene horizon (Fig. 16). Four faults in this subgroup dip towards the south, towards the centre of the deep part of the minibasin described above, whereas one dips to the north (Fig. 4). A5-9 have down-dip heights which range between 400–670 m and maximum lengths of 930–1730 m, yielding aspect ratios of 2.1 – 3.9 (Fig. 9). The maximum throw on these faults are generally less than that observed on A1-4 (i.e. maximum throws of ~10 - 15 m; Fig. 15 a).

#### *4.3.2 Interpretations*

Since the arcuate faults closely parallel the outer rim of the deep part of the minibasin (Fig. 4) we suggest they formed to accommodate outer arc-style bending and stretching of the minibasin-fill during differential subsidence and salt withdrawal (Fig. 16); geometrically similar faults are observed in association with mobile mud withdrawal (Stewart, 2006). We propose these faults became overdisplaced for two reasons. Firstly, the larger faults in the first subgroup (A1 - 4) terminate very near the salt-sediment interface suggesting that these faults became restricted laterally due to not being able to propagate into the weak salt (e.g. Tvedt et al., 2013). Thus, resulting in these faults becoming overdisplaced as throw accrual continues under laterally restricted tips. Secondly, the shallower second subgroup are more closely spaced than other faults within the extensional array and are sub-parallel (Fig. 4a). We propose that these faults experienced mechanical interactions between their fault tips, which resulted in lateral restriction of their growth and overdisplacement. While the cause (i.e fault interaction) for fault restriction differs to that of the larger arcuate faults (i.e. salt interaction), the result of overdisplacement is the same (e.g. Crider and Pollard, 1998, Martel, 1999, Nicol et al., 2017).

## 5 Discussion and Implications

### *5.1 Origin and kinematics of planar normal faults; the case for tip restriction by host rock properties*

The occurrence of throw maxima within Miocene and Pliocene strata suggest the planar faults nucleated within Neogene stratigraphy (Fig. 10) (Hongxing and Anderson, 2007). Whereas all other planar faults propagated as blind structures, F1 represented a surface-breaching growth fault during at least the Pliocene (Fig. 10). During the Middle Miocene, salt and overburden translation rates increased significantly from *c.* 0.2 to 1 mm/yr within the Outer Kwanza Basin, principally due to margin uplift (Hudec and Jackson, 2004, Evans and Jackson, 2019). Depending on the structural position on the margin, this resulted in extensional (i.e. typically in updip, proximal locations) or contractional (i.e. typically in downdip, distal locations) deformation of salt and its overburden (Hudec and Jackson, 2004, Evans and Jackson, 2019). Despite our study area being in the present-day transitional domain (Fig. 1), increases in downdip salt flux could have resulted in local extension of this area due to outer-arc bending and translation across the base-salt relief (Evans and Jackson, 2019). The planar faults may therefore have formed in the Middle Miocene in response to this increased rate of basinward translation of salt and its overburden, eventually breaching the seabed in the Pliocene, as evidenced by the presence of the growth strata in the hanging wall of F1 (Evans and Jackson, 2019).

Field-based studies and modelling results show that mechanical stratigraphy can influence the growth and ultimate geometry of normal faults; e.g. multi-layered sequences defined by different rock competencies controls, down-dip linkage, fault restriction and fault aspect ratio (e.g. Wilkins and Gross, 2002, Soliva and Benedicto, 2005, Schöpfer et al., 2006). For example, Nicol et al. (1996) suggest vertically restricted faults display greater aspect ratios.

More recent work proposes various mechanisms by which vertical restriction might occur, showing that faults growing in mechanically more homogenous host rocks assume circular to elliptical shapes throughout their lives, whereas those in multi-layered sequences can have their vertical growth impeded, thus growing from a circular to an elliptical geometry, resulting in an increase in aspect ratio (Fig. 12) (Soliva et al., 2005a, Soliva and Benedicto, 2005, Soliva et al., 2006). One consequence of the latter style of fault growth is the development of high throw gradients at the restricted (vertical) tip (Fig. 8d and e) (Wilkins and Gross, 2002). Within the planar fault group, F3 and F4 have relatively high aspect ratios (3.5 and 5.2, respectively) and high throw gradients (0.12 and 0.11, respectively) at their lower tips; these values are an order-of-magnitude greater than those of F1 and F2 (0.01). The migration of throw to the restricted tip and consequent high throw gradients is shown by the presence of their throw maxima being slightly offset towards their lower tips, which is characteristic of mechanically bound faults (Fig. 8 d and e, and 10) (e.g. Wilkins and Gross, 2002, Soliva and Benedicto, 2005, Soliva et al., 2005b). In contrast, relatively closely (< 1 km) spaced faults within the bifurcating fault group, which have throw maxima of > 30 m and that offset the MTC, do not have these geometric characteristics (Fig. 11). This pattern, where only faults with $T_{max}$ > 30 m offset the MTC, can be observed in the arcuate fault group in the extensional array (Fig. 11b). An important observation is that, despite being < 1 km from F3 and 4 and although they offset similar stratigraphy (Fig. 5), the lower tips of F1 and 2 lie above the MTC; as a result, these faults do not have the same high aspect ratios or throw gradients at their lower tips (Fig. 5; 7 and 9).

The variable geometric relationships between the faults and the MTC suggests that it acted as a mechanical layer, restricting the downward and upward propagation of the fault tips and overall enlargement of the surfaces of faults that ultimately only accumulated only < 30 m maximum throw (Fig. 11 b). This resulted in higher aspect ratios and lower tip throw gradients on those faults not able to propagate, as well as influencing the growth, geometry and throw distribution of bifurcating faults (Fig. 12 and 14). Because drilling data are not available to determine the MTC lithology or mechanical properties, we do not know if this unit retarded tip propagation by: (i) acting as a relatively stiff layer that was hard to strain; or (ii) acting in a ductile manner, with strain being internally distributed in a more diffuse manner. The latter case has been observed in field-based studies of normal faulted, mechanically layered host rocks, with faults seemingly nucleating and propagating only in more competent, stiff layers (typically >0.5 m thick) (Soliva et al., 2005b). Underlying and overlying, more compliant layers (<0.5 m thick) behave in a ductile manner and are characterised by diffuse strain and high strain gradients. Faults essentially decouple in these layers, with high aspect ratios and underdisplaced fault populations arising as a function of ‘forced’ propagation within the stiff layers. We propose that this case may also apply at a substantially larger, seismic-scale, such as that documented here. Deep water MTC’s are predominantly mudstone-dominated (Wu et al., 2019) meaning that it could be the case that they act in a ductile manner with strain being more diffuse, as documented in mechanically heterogeneous faulted sequences (e.g. Bürgmann et al., 1994, e.g. Nicol et al., 1996, Wilkins and Gross, 2002, Soliva and Benedicto, 2005, Soliva et al., 2005b, Soliva et al., 2005a, Roche et al., 2012). In the absence of drilling data, we propose that either of these hypotheses could be the case for the MTC’s mechanical control on fault growth.

*5.2 Kinematics of bifurcating faults; overcoming tip restriction and continued fault growth*

Fault linkage and bifurcation control the distribution of throw on normal fault surfaces (e.g. Peacock and Sanderson, 1991, Dawers and Anders, 1995, Mansfield and Cartwright, 2001, Peacock, 2002, Soliva and Benedicto, 2004, Soliva et al., 2008). We noted that the laterally restricted branchline of F7 occurs at the top of the Miocene MTC, and that the throw maximum also lies at this structural and stratigraphic level. The throw maximum is restricted to the larger, rearward (i.e. footwall side) fault and does not continue onto the frontal (i.e. hangingwall side) splay (Fig. 13b). In section 5.1 we discussed that the vertical restriction of the lower tips within the planar fault group resulted in high throw gradients (Wilkins and Gross, 2002, Jackson et al., 2014). If a similar process occurred during growth of the fault F7, which bifurcates upwards, it could follow that pinned precursor segments nucleated above the MTC as physically separate structures, with high stressing building-up at their lower tips before they were able to link and propagate onward, resulting in the present throw pattern (Fig. 13b and 14a). The same process could occur for a segmented fault system nucleating *below* and ultimately propagating upwards through a mechanical layer (Wilkins and Gross, 2002).

An alternative interpretation for the throw patterns on F7 is based on our observation that the main, rearward segment accommodates a laterally extensive, sub-horizontal throw maxima, whereas the frontal splay has overall lower throw values and lacks a discrete throw maximum (Fig. 13). Thus, we may interpret that the main fault surface nucleated above the MTC and started to grow before the splay, becoming temporarily mechanically pinned along the MTC, resulting in the development of throw maxima before propagating further downwards (Wilkins and Gross, 2002) (Fig. 13). The splay segment, which also nucleated above the MTC, may not have achieved the critical tip stresses required for onwards propagation, instead linking down-dip with the main fault surface near the top of the MTC (Wilkins and Gross, 2002, Soliva and Benedicto, 2005, Soliva et al., 2005b) (Fig. 13).

Bifurcating fault F6 shows a distinct concentration of high throw near the MTC (Fig. 13a); this is consistent with the hypothesis of stress and strain concentration at the MTC prior to onward fault propagation (Fig. 14). Moreover, a second distinct area of high throw occurs on the frontal fault of F6, immediately east of the relay zone (Fig. 13a). This is consistent with throw distributions typically seen within relay zones, where tip interaction occurs between adjacent, upward-propagating segments (Peacock and Sanderson, 1991, Trudgill and Cartwright, 1994, Peacock and Sanderson, 1994, Peacock, 2002, Long and Imber, 2012, Freitag et al., 2017). Fault bifurcation can occur as a result of stress field reorientation or non-uniformity, as well as irregular tip-line propagation due to intra-host rock mechanical heterogeneities, such as an intra-stratal MTC (Soliva et al., 2008). This would explain the bifurcation and position of the branchline on the top of the MTC (Fig. 5a and 13). Our data suggest that only faults that accumulated > 30 m of throw were able to propagate through the MTC; below this value, the tips were pinned due to the build-up of insufficient tip stresses to allow onward propagation (Fig. 11 a and b) (Wilkins and Gross, 2002).

### *5.3 Normal fault growth and D-L scaling relationships*

D-L scaling relationships derived from global datasets have historically been used to support a normal fault growth model by synchronous lengthening and displacement accumulation (i.e. 'propagating model'; Childs et al., 2017, Rotevatn et al., 2018); (See also e.g. Watterson, 1986, Walsh and Watterson, 1988, Walsh et al., 2002). More recently, however, studies using 3D seismic reflection data have integrated stratigraphic data in an otherwise purely geometrical analyses. This has given rise to an alternative fault growth model that states fault lengthening (which may include linkage of initially isolated segments) occurs before the accumulation of significant displacement (i.e. 'constant-length model'; Jackson and Rotevatn, 2013, Childs et al., 2017, Rotevatn et al., 2019, Nicol et al., 2020).

We show here that host-rock heterogeneities, and near- and far-field stress regimes and their interactions, can all result in the formation of under- or over-displaced faults (i.e. faults that significantly deviate from global D-L scaling relationships and thus produce scatter within these datasets), and/or faults with anomalously low or high aspect ratios (Cowie and Scholz, 1992a, Dawers and Anders, 1995, Peacock, 2002, Soliva and Benedicto, 2005, Soliva et al., 2005b, Soliva et al., 2005a). This is in addition to fault linkage, which typically results in underdisplaced faults likely characterised by anomalously low aspect ratios (Cartwright et al., 1995). Our study shows how detailed analysis of largely blind faults of varying sizes developing within the same overall tectono-stratigraphic setting can shed light on the kinematics of fault growth; such studies can complement those focused on growth faults flanked by syn-kinematic strata (e.g. Tvedt et al., 2013, Duffy et al., 2015, e.g. Jackson et al., 2017). A key observation is that the studied faults would fall within the general scatter present in global D-L scaling datasets (Fig. 2), and that this would mask the not insignificant variability in their geometric properties (i.e. D-L relationship, aspect ratio) and inferred growth patterns, and the relationship of these to local stratigraphic factors (i.e. an intra-stratal MTC).

## 6.0 Conclusions

3D seismic reflection data from the Outer Kwanza Basin, offshore Angola image a basement-decoupled normal fault population that deform a clastic-dominated, deep-water succession. These faults are up to 6.3 km long, 1.9 km tall, and have up to 44 m of throw. Aspect ratios (i.e. fault height to fault length), maximum throw, and lower-tip throw gradients vary between faults, being greater (aspect ratio up to 5.2; maximum throw <30 m; throw gradients up to 0.12) for faults that terminate downwards at an intra-stratal mass-transport complex (MTC) than those that offset it (aspect ratio up to 3.6; maximum throw >30 m; throw gradients up to 0.08). We interpret that the faults nucleated above and propagated down towards the MTC. Upon encountering this unit, which we infer was weaker than the encasing strata, tip propagation was halted until tip stresses were sufficiently high to breach it. We suggest that such stresses were reached when a fault accumulated a maximum throw of at least 30 m. The displacement-length (D-L) relationship for all faults fall within the general scatter present in global D-L scaling datasets, regardless of their geometry or growth patterns. In the absence of growth strata, D-L scaling relationships must be used with caution when studying fault kinematics, given the role mechanical stratigraphy plays in controlling fault propagation, size, finite throw (or displacement), and geometry. Mechanical stratigraphy therefore has a key control on the growth of large, seismic-scale normal in a similar way to that observed for far smaller structures.

## Acknowledgements

We would like to thank the significant guidance and comments of the reviewers and editors, notably C. J. Ebinger and Andy Green. We thank the NERC Centre for Doctoral Training in Oil and Gas for the provision of funding to the PhD research of David Redpath. We also thank CGG for making these data available for academic use. The data can be accessed by direct request to CGG (https://www.cgg.com/multi-client-data/multi-client-seismic), upon signing of a confidentiality agreement. We also thank Schlumberger for providing access to Petrel software.

## References

ATHMER, W. & LUTHI, S. M. 2011. The effect of relay ramps on sediment routes and deposition: A review. *Sedimentary Geology,* 242**,** 1-17.

BATE, R. H., CAMERON, N. R. & BRANDÃO, M. G. P. 2001. The lower cretaceous (Pre-Salt) lithostratigraphy of the Kwanza Basin, Angola, *Newsletter on Stratigraphy,* 38, 117-127.

BAUDON, C. & CARTWRIGHT, J. 2008. The kinematics of reactivation of normal faults using high resolution throw mapping. *Journal of Structural Geology,* 30**,** 1072-1084.

BODVARSSON, G., BENSON, S. & WITHERSPOON, P. 1982. Theory of the development of geothermal systems charged by vertical faults. *Journal of Geophysical Research: Solid Earth,* 87**,** 9317-9328.

BRICE, S. E., COCHRAN, M. D., PARDO, G. & EDWARDS, A. D. 1982. Tectonics and Sedimentation of the South Atlantic Rift Sequence: Cabinda, Angola. *AAPG Memoirs,* 34. Studies in Continental Margin Geology. *In:* WATKINS, J. S. & DRAKE, C. L. (eds.).

BÜRGMANN, R., POLLARD, D. D. & MARTEL, S. J. 1994. Slip distributions on faults: effects of stress gradients, inelastic deformation, heterogeneous host-rock stiffness, and fault interaction. *Journal of Structural Geology,* 16, 1675-1690.

CARTWRIGHT, J. A., TRUDGILL, B. D. & MANSFIELD, C. S. 1995. Fault growth by segment linkage: an explanation for scatter in maximum displacement and trace length data from the Canyonlands Grabens of SE Utah. *Journal of Structural Geology,* 17, 1319-1326.

CHILDS, C., HOLDSWORTH, R. E., JACKSON, C. A. L., MANZOCCHI, T., WALSH, J. J. & YIELDING, G. 2017. Introduction to the geometry and growth of normal faults. *Geological Society, London, Special Publications,* 439, 1.

CHILDS, C., NICOL, A., WALSH, J. J. & WATTERSON, J. 2003. The growth and propagation of synsedimentary faults. *Journal of Structural Geology,* 25, 633-648.

COLLANEGA, L., JACKSON, C., BELL, R., COLEMAN, A., LENHART, A. & BREDA, A. 2018. Normal fault growth influenced by basement fabrics: the importance of preferential nucleation from pre-existing structures. *Basin Research*, 31, 659-687

CORBEL, S., SCHILLING, O., HOROWITZ, F., REID, L., SHELDON, H., TIMMS, N. & WILKES, P. Identification and geothermal influence of faults in the Perth metropolitan area, Australia. *Thirty-Seventh Workshop on Geothermal Reservoir Engineering, 2012. Stanford University California, 8.*

COWIE, P. A. & SCHOLZ, C. H. 1992a. Displacement-length scaling relationship for faults: data synthesis and discussion. *Journal of Structural Geology,* 14, 1149-1156.

COWIE, P. A. & SCHOLZ, C. H. 1992b. Growth of faults by accumulation of seismic slip. *Journal of Geophysical Research: Solid Earth,* 97, 11085-11095.

CRIDER, J. G. & POLLARD, D. D. 1998. Fault linkage: Three-dimensional mechanical interaction between echelon normal faults. *Journal of Geophysical Research: Solid Earth,* 103, 24373-24391.

DAWERS, N. H. & ANDERS, M. H. 1995. Displacement-length scaling and fault linkage. *Journal of Structural Geology,* 17, 607-614.

DUFFY, O., BELL, R., JACKSON, C., L. GAWTHORPE, R. & S. WHIPP, P. 2015. Fault Growth and Interactions in a Multiphase Rift Fault Network: Horda Platform, Norwegian North Sea, *Journal of Structural Geology*, 80, 99-119.

ELIET, P. & GAWTHORPE, R. 1995. Drainage development and sediment supply within rifts, examples from the Sperchios basin, central Greece. *Journal of the Geological Society,* 152, 883-893.

EVANS, S. L. & JACKSON, C. A.-L. 2019. Base-salt relief controls salt-related deformation in the Outer Kwanza Basin, offshore Angola. *Basin Research*, 32, 668-687.

FAIRLEY, J. P. & HINDS, J. J. 2004. Rapid transport pathways for geothermal fluids in an active Great Basin fault zone. *Geology,* 32, 825-828.

FERRILL, D. A. & MORRIS, A. P. 2008. Fault zone deformation controlled by carbonate mechanical stratigraphy, Balcones fault system, Texas. *AAPG Bulletin*, 92 (3), 359-380

FERRILL, D. A., MORRIS, A. P., MCGINNIS, R. N., SMART, K. J., WIGGINTON, S. S., HILL, N. J. 2017. Mechanical stratigraphy and normal faulting. *Journal of Structural Geology*, 94, 275-302.

FRASER, A.J., HILKEWICH, D., SYMS, R., PENGE, J., RAPOSO, A. & SIMON, G. 2005. Angola Block 18: a deep-water exploration success story. *Geological Society of London, Petroleum Geology Conference series*, 6 (1), 1199-1216.

FREITAG, U. A., SANDERSON, D. J., LONERGAN, L. & BEVAN, T. G. 2017. Comparison of upwards splaying and upwards merging segmented normal faults. *Journal of Structural Geology,* 100, 1-11.

GAWTHORPE, R. L. & HURST, J. M. 1993. Transfer zones in extensional basins: their structural style and influence on drainage development and stratigraphy. *Journal of the Geological Society*, 150, 1137-1152.

GAWTHORPE, R. L. & LEEDER, M. R. 2000. Tectono-sedimentary evolution of active extensional basins. *Basin Research,* 12, 195-218.

GHALAYINI, R., DANIEL, J.-M., NADER, F. & HOMBERG, C. 2016. Predicting reservoir intervals by looking at fault data: An exploration tool in frontier basins. *International Conference and Exhibition, Barcelona, Spain, 3-6 April 2016.*

GIBBS, A. D. 1984. Structural evolution of extensional basin margins. *Journal of the Geological Society,* 141, 609-620.

GROSHONG JR., R. H. 2006. 3-D Structural Geology. *Springer-Verlag Berlin Heidelberg,* 305-371.

GUPTA, A. & SCHOLZ, C. H. 2000. A model of normal fault interaction based on observations and theory. *Journal of Structural Geology,* 22, 865-879.

HONGXING, G. & ANDERSON, J. K. 2007. Fault throw profile and kinematics of Normal fault: conceptual models and geologic examples. *Geological Journal of China Universities,* 13, 75-88.

HOWLETT, D. M., GAWTHORPE, R. L., GE, Z., ROTEVATN, A. & JACKSON, C. A.-L. 2020. Turbidites, topography and tectonics: Evolution of submarine channel-lobe systems in the salt-influenced Kwanza Basin, offshore Angola. *Basin Research.*

HUDEC, M. & JACKSON, M. 2003. Structural segmentation, inversion, and salt tectonics on a passive margin: Evolution of the Inner Kwanza Basin, Angola. *The Geological Society of America Bulletin,* 115, 641.

HUDEC, M. & JACKSON, M. 2004. Regional restoration across the Kwanza Basin, Angola: Salt tectonics triggered by repeated uplift of a metastable passive margin. *AAPG Bulletin,* 88,971-990.

JACKSON, C. A.-L., CARRUTHERS, D. T., MAHLO, S. N. & BRIGGS, O. 2014. Can polygonal faults help locate deep-water reservoirs? *AAPG Bulletin,* 98, 1717-1738.

JACKSON, C. A. L., BELL, R. E., ROTEVATN, A. & TVEDT, A. B. M. 2017. Techniques to determine the kinematics of synsedimentary normal faults and implications for fault growth models. *Geological Society, London, Special Publications*, 439, 187.

JACKSON, C. A. L. & ROTEVATN, A. 2013. 3D seismic analysis of the structure and evolution of a salt-influenced normal fault zone: A test of competing fault growth models. *Journal of Structural Geology,* 54, 215-234.

JACKSON, M. P. A. & HUDEC, M. R. 2008. Interplay of Basement, Salt Tectonics, and Sedimentation in the Kwanza Basin, Angola *AAPG International Conference and Exhibition 2008*.

JACKSON, M. P. A., HUDEC, M. R. & HEGARTY, K. A. 2005. The great West African Tertiary coastal uplift: Fact or fiction? A perspective from the Angolan divergent margin. *Tectonics,* 24, 6.

KARNER, G. D. & GAMBÔA, L. A. P. 2007. Timing and origin of the South Atlantic pre-salt sag basins and their capping evaporites. *Geological Society, London, Special Publications,* 285, 15.

KHALIL, S. M. & MCCLAY, K. R. 2017. 3D geometry and kinematic evolution of extensional fault-related folds, NW Red Sea, Egypt. *Geological Society, London, Special Publications,* 439, 109.

LAUBACH, S. E., OLSON, J. E. & GROSS, M. R. 2009. Mechanical and fracture stratigraphy. *AAPG Bulletin,* 93 (11), 1413-1426.

LEEDER, M. R. & GAWTHORPE, R. L. 1987. Sedimentary models for extensional tilt-block/half-graben basins. *Geological Society, London, Special Publications,* 28**,** 139-152.

LOHR, T., M. KRAWCZYK, C., ONCKEN, O. & TANNER, D. 2008. Evolution of a fault surface from 3D attribute analysis and displacement measurements. *Jounral of Structural Geology,* 30, 690-700.

LONG, J. J. & IMBER, J. 2012. Strain compatibility and fault linkage in relay zones on normal faults. *Journal of Structural Geology,* 36**,** 16-26.

MANSFIELD, C. & CARTWRIGHT, J. 2001. Fault growth by linkage: Observations and implications from analogue models. *Journal of Structural Geology,* 23, 745-763.

MARRETT, R. & ALLMENDINGER, R. W. 1990. Kinematic analysis of fault-slip data. *Journal of Structural Geology,* 12**,** 973-986.

MARTEL, S. J. 1999. Mechanical controls on fault geometry. *Journal of Structural Geology,* 21**,** 585-596.

MARTON, L. G., TARI, G. C. & LEHMANN, C. T. 2000. Evolution of the Angolan passive margin, West Africa, with emphasis on post-salt structural styles. *Geophysical Monograph-American Geophysical Union,* 115**,** 129-150.

MCCLAY, K. R. 1990. Extensional fault systems in sedimentary basins: a review of analogue model studies. *Marine and Petroleum Geology,* 7**,** 206-233.

MCLEOD, A. E., DAWERS*, N. H. & UNDERHILL, J. R. 2000. The propagation and linkage of normal faults: insights from the Strathspey–Brent–Statfjord fault array, northern North Sea. *Basin Research,* 12**,** 263-284.

MORLEY, C. 2017. The impact of multiple extension events, stress rotation and inherited fabrics on normal fault geometries and evolution in the Cenozoic rift basins of Thailand. *Geological Society, London, Special Publications,* 439**,** 413-445.

MORLEY, C. K. 2007. Development of crestal normal faults associated with deepwater fold growth. *Journal of Structural Geology,* 29**,** 1148-1163.

MOSCARDELLI, L. & WOOD, L. 2008. New classification system for mass transport complexes in offshore Trinidad. *Basin Research,* 20**,** 73-98.

NICOL, A., CHILDS, C., WALSH, J., MANZOCCHI, T. & SCHÖPFER, M. 2017. Interactions and growth of faults in an outcrop-scale system. *Geological Society, London, Special Publications,* 439**,** 23-39.

NICOL, A., WALSH, J., BERRYMAN, K. & NODDER, S. 2005. Growth of a normal fault by the accumulation of slip over millions of years. *Journal of Structural Geology,* 27**,** 327-342.

NICOL, A., WALSH, J., CHILDS, C. & MANZOCCHI, T. 2020. Chapter 6 - The growth of faults. *In:* TANNER, D. & BRANDES, C. (eds.) *Understanding Faults.* Elsevier.

NICOL, A., WATTERSON, J., WALSH, J. J. & CHILDS, C. 1996. The shapes, major axis orientations and displacement patterns of fault surfaces. *Journal of Structural Geology,* 18**,** 235-248.

PEACOCK, D. & SANDERSON, D. 1994. Geometry and development of relay ramps in normal fault systems. *AAPG bulletin,* 78**,** 147-165.

PEACOCK, D. C. P. 2002. Propagation, interaction and linkage in normal fault systems. *Earth-Science Reviews,* 58**,** 121-142.

PEACOCK, D. C. P. & SANDERSON, D. J. 1991. Displacements, segment linkage and relay ramps in normal fault zones. *Journal of Structural Geology,* 13**,** 721-733.

POLIT, A. T., SCHULTZ, R. A. & SOLIVA, R. 2009. Geometry, displacement–length scaling, and extensional strain of normal faults on Mars with inferences on mechanical stratigraphy of the Martian crust. *Journal of Structural Geology,* 31**,** 662-673.

REEVE, M. T., BELL, R. E., DUFFY, O. B., JACKSON, C. A.-L. & SANSOM, E. 2015. The growth of non-colinear normal fault systems; What can we learn from 3D seismic reflection data? *Journal of Structural Geology,* 70**,** 141-155.

REILLY, C., NICOL, A., WALSH, J. J. & KROEGER, K. F. 2016. Temporal changes of fault seal and early charge of the Maui Gas-condensate field, Taranaki Basin, New Zealand. *Marine and Petroleum Geology,* 70**,** 237-250.

ROCHE, V., HOMBERG, C. & ROCHER, M. 2012. Fault displacement profiles in multilayer systems: from fault restriction to fault propagation. *Terra Nova,* 24**,** 499-504.

ROTEVATN, A., FOSSEN, H., HESTHAMMER, J., AAS, T. E. & HOWELL, J. A. 2007. Are relay ramps conduits for fluid flow? Structural analysis of a relay ramp in Arches National Park, Utah. *Geological Society, London, Special Publications,* 270**,** 55.

ROTEVATN, A., JACKSON, C. A. L., TVEDT, A. B. M., BELL, R. E. & BLÆKKAN, I. 2018. How do normal faults grow? *Journal of Structural Geology*.

ROTEVATN, A., JACKSON, C. A. L., TVEDT, A. B. M., BELL, R. E. & BLÆKKAN, I. 2019. How do normal faults grow? *Journal of Structural Geology,* 125**,** 174-184.

SCHÖPFER, M. P. J., CHILDS, C. & WALSH, J. J. 2006. Localisation of normal faults in multilayer sequences. *Journal of Structural Geology,* 28**,** 816-833.

SCHULTZ, R. 1999. Understanding the process of faulting: selected challenges and opportunities at the edge of the 21st century. *Journal of Structural Geology,* 21**,** 985-993.

SERIÉ, C., HUUSE, M., SCHØDT, N. H., BROOKS, J. M. & WILLIAMS, A. 2017. Subsurface fluid flow in the deep-water Kwanza Basin, offshore Angola. *Basin Research,* 29**,** 149-179.

SOLIVA, R. & BENEDICTO, A. 2004. A linkage criterion for segmented normal faults. *Journal of Structural Geology,* 26**,** 2251-2267.

SOLIVA, R. & BENEDICTO, A. 2005. Geometry, scaling relations and spacing of vertically restricted normal faults. *Journal of Structural Geology,* 27**,** 317-325.

SOLIVA, R., BENEDICTO, A., SCHULTZ, R. A., MAERTEN, L. & MICARELLI, L. 2008. Displacement and interaction of normal fault segments branched at depth: Implications for fault growth and potential earthquake rupture size. *Journal of Structural Geology,* 30**,** 1288-1299.

SOLIVA, R., BENEDICTO, A., VERGÉLY, P. & RIVES, T. 2005a. Mechanical control of a lithological alternation on normal fault morphology, growth and reactivation. *Bulletin de la Société Géologique de France,* 176**,** 329-342.

SOLIVA, R. & SCHULTZ, R. A. 2008. Distributed and localized faulting in extensional settings: insight from the North Ethiopian Rift–Afar transition area. *Tectonics,* 27.

SOLIVA, R., SCHULTZ, R. A. & BENEDICTO, A. 2005b. Three-dimensional displacement-length scaling and maximum dimension of normal faults in layered rocks. *Geophysical Research Letters,* 32.

SOLIVA, S., ANTONIO, B. & LAURENT, M. 2006. Spacing and linkage of confined normal faults: Importance of mechanical thickness. *Journal of Geophysical Research: Solid Earth,* 111.

SPATHOPOULOS, F. 1996. An insight on salt tectonics in the Angola Basin, South Atlantic. *Geological Society, London, Special Publications,* 100**,** 153.

STEWART, S. A. 2006. Implications of passive salt diapir kinematics for reservoir segmentation by radial and concentric faults. *Marine and Petroleum Geology,* 23, 843-853.

TORABI, A., ALAEI, B. & LIBAK, A. 2019. Normal fault 3D geometry and displacement revisited: Insights from faults in the Norwegian Barents Sea. *Marine and Petroleum Geology,* 99**,** 135-155.

TRUDGILL, B. D. & CARTWRIGHT, J. A. 1994. Relay-ramp forms and normal-fault linkages, Canyonlands National Park, Utah. *GSA Bulletin,* 106**,** 1143-1157.

TVEDT, A. B. M., ROTEVATN, A. & JACKSON, C. A. L. 2016. Supra-salt normal fault growth during the rise and fall of a diapir: Perspectives from 3D seismic reflection data, Norwegian North Sea. *Journal of Structural Geology,* 91**,** 1-26.

TVEDT, A. B. M., ROTEVATN, A., JACKSON, C. A. L., FOSSEN, H. & GAWTHORPE, R. L. 2013. Growth of normal faults in multilayer sequences: A 3D seismic case study from the Egersund Basin, Norwegian North Sea. *Journal of Structural Geology,* 55**,** 1-20.

WALSH, J. J., BAILEY, W. R., CHILDS, C., NICOL, A. & BONSON, C. G. 2003. Formation of segmented normal faults: a 3-D perspective. *Journal of Structural Geology,* 25**,** 1251-1262.

WALSH, J. J., NICOL, A. & CHILDS, C. 2002. An alternative model for the growth of faults. *Journal of Structural Geology,* 24**,** 1669-1675.

WALSH, J. J. & WATTERSON, J. 1987. Distributions of cumulative displacement and seismic slip on a single normal fault surface. *Journal of Structural Geology,* 9**,** 1039-1046.

WALSH, J. J. & WATTERSON, J. 1988. Analysis of the relationship between displacements and dimensions of faults. *Journal of Structural Geology,* 10**,** 239-247.

WALSH, J. J. & WATTERSON, J. 1991. Geometric and kinematic coherence and scale effects in normal fault systems. *Geological Society, London, Special Publications,* 56**,** 193-203.

WATTERSON, J. 1986. Fault dimensions, displacements and growth. *Pure And Applied Geophysics,* 124**,** 365-373.

WHIPP, P., JACKSON, C. L., GAWTHORPE, R., DREYER, T. & QUINN, D. 2014. Normal fault array evolution above a reactivated rift fabric; a subsurface example from the northern Horda Platform, Norwegian North Sea. *Basin Research,* 26**,** 523-549.

WILKINS, S. J. & GROSS, M. R. 2002. Normal fault growth in layered rocks at Split Mountain, Utah: influence of mechanical stratigraphy on dip linkage, fault restriction and fault scaling. *Journal of Structural Geology,* 24**,** 1413-1429.

WILKINSON, M., ROBERTS, G. P., MCCAFFREY, K., COWIE, P. A., FAURE WALKER, J. P., PAPANIKOLAOU, I., PHILLIPS, R. J., MICHETTI, A. M., VITTORI, E., GREGORY, L., WEDMORE, L. & WATSON, Z. K. 2015. Slip distributions on active normal faults measured from LiDAR and field mapping of geomorphic offsets: an example from L'Aquila, Italy, and implications for modelling seismic moment release. *Geomorphology,* 237**,** 130-141.

WILLEMSE, E. J., POLLARD, D. D. & AYDIN, A. 1996. Three-dimensional analyses of slip distributions on normal fault arrays with consequences for fault scaling. *Journal of Structural Geology,* 18**,** 295-309.

WORTHINGTON, R. P. & WALSH, J. J. 2017. Timing, growth and structure of a reactivated basin-bounding fault. *Geological Society, London, Special Publications,* 439**,** 511.

WU, N., JACKSON, C., JOHNSON, H. & HODGSON, D. 2019. Lithological, petrophysical and seal properties of mass-transport complexes (MTCs), northern Gulf of Mexico. *Basin Research,* 32, 1300-1327.

XU, S., SAMANIEGO, Á. F. N., ÁLVAREZ, S. A. A. & MARTÍNEZ, L. M. C. 2011. Structural analysis of a relay ramp in the Querétaro graben, central Mexico: Implications for relay ramp development. *Revista mexicana de ciencias geológicas,* 28**,** 275-289.

YOUNG, M. J., GAWTHORPE, R. L. & HARDY, S. 2001. Growth and linkage of a segmented normal fault zone; the Late Jurassic Murchison–Statfjord North Fault, northern North Sea. *Journal of Structural Geology,* 23**,** 1933-1952.

**Figure 1:** (Top left) A location map of the CGG 3D PDSM survey showing the 70 km2 study area and the regional section. (Top right) A seafloor depth structure map highlighting the presence of the N-S trending salt wall and the minibasin on its western flank, which characterise our study area. (Bottom) A regional cross-section outlining the structure and location of our study area in the Outer Kwanza Basin on the Angolan passive margin.

**Figure 2:** D-L data for extensional faults on a log-log plot extracted from global studies (blue): (Nicol et al., 1996, McLeod et al., 2000, Young et al., 2001, Nicol et al., 2005, Morley, 2007, Baudon and Cartwright, 2008, Xu et al., 2011, Tvedt et al., 2013, Whipp et al., 2014, Reeve et al., 2015, Duffy et al., 2015, Tvedt et al., 2016, Ghalayini et al., 2016, Reilly et al., 2016, Khalil and McClay, 2017, Morley, 2017, Worthington and Walsh, 2017, Torabi et al., 2019)**.** The D-L fault data presented within this study are also shown (orange). Note that the D-L data sit within global D-L patterns and, that on this scale, adhere to scaling laws (i.e. D = *c*L*n*), despite that the data presented revealing deviations from D-L scaling relationships in their geometry and growth histories (see text for full discussion).

**Figure 3:** A seismic overview of the structure and stratigraphy of the study area, highlighting the key stratigraphic and structural elements in this study. Data courtesy of CGG Multi-Client.

**Figure 4:** (a-d) Depth structure maps of the Intra-Pliocene, Top Miocene, Top Eocene and Top Albian surface, respectively. The temporal and spatial presence of each of the studied

faults is also highlighted on each of the structure maps. The Top Albian surface is not offset by any of the faults and shows the location of seismic sections for figure 5.

**Figure 5:** (a) Left. (b) Right. Seismic cross-sections of planar (F1-4) and bifurcated (F6-7) faults showing their dip and interaction with each of the key Intra-Pliocene, Top Miocene and Top MTC surfaces, shown with depth respectively. Here, the bifurcated faults show bifurcating upward fault segments with narrow relay zones and offset the Top MTC horizon. Data courtesy of CGG Multi-Client.

**Figure 6:** An overview of fault terminology; including the defined terms for calculating aspect ratio (top) and determining the geometry of a fault (bottom).

**Figure 7:** A variance extraction (-1400 m) of meandering channels (right). Seismic sections of the erosional channels observed in the variance extraction within the shallow stratigraphy of the area (*c.* 200-250m below seabed). The erosional bases of these channels erode the upper tips of faults (e.g. F3). In the case where upper fault tips offset the channel deposits (e.g. F4, F6 and F7) it is likely any previous growth packages of near-seabed growth have been eroded. Data courtesy of CGG Multi-Client.

**Figure 8:** (a) A variance extraction of the Intra-Pliocene surface and the locations of F1-4. Strike projections for F1-4, respectively. They display the geometry of, and throw distribution on, the fault surfaces with the Intra-Pliocene and Top Miocene surfaces, respectively with depth. Unrestricted faults (F1; 8b, and F2; 8c) display throw maxima in Pliocene stratigraphy which decrease towards their tips. Restricted faults (F3; 8d, and F4; 8e) display throw maxima positioned towards their lower tips in Miocene stratigraphy. The aspect ratios for F1-2 are 0.01, and are 0.12 and 0.11 for F3-4, respectively. The aspect ratios for F1-2 is 2.7, while F3 and F4 have greater aspect ratios of 3.7 and 5.2, respectively.

**Figure 9:** Fault height - length data for all fault groups within the studied array. Overall, a trend is observed of fault height increasing proportionally with fault length. However, faults which tip out down dip at the Top MTC surface and have high aspect ratios (F3-4) show increasing fault length without a proportional increase in fault height (red), as predicted for vertically restricted faults (Fig. 12).

**Figure 10:** A seismic section of the position of unrestricted faults (F1-2) within the stratigraphy. Their lower tips do not interact with the MTC layer. A t-z plot for F1 where the EI on the upper tip is *c.* 1.2 (left). T-z plots (F1-4) showing that restricted faults exhibit throw maxima in Miocene stratigraphy and unrestricted faults exhibit throw maxima in Pliocene stratigraphy (right). Data courtesy of CGG Multi-Client.

**Figure 11:** (a) A seismic cross-section showing the tips of F3-4 tipping out downdip on top of the MTC surface and the adjacent bifurcating faults (F6-7) offsetting the Top MTC surface. Above, the maximum throw of the respective faults are displayed and the proposed accumulated strain needed to overcome the threshold for onward growth through the MTC (grey box). (b) Throw-length data for the fault array displaying that faults with maximum throws > 30 m offset the MTC, while faults with throw values < 30 m which interact with the MTC are vertically restricted. T-x regression analysis for the array's data also suggests the constant length model for fault growth [i.e. T>0 where L=0]. (c) T-x plots for faults restricted by the MTC (F2-3) and some which achieve onward propagation (F6-7, A4). Data courtesy of CGG Multi-Client.

**Figure 12:** A sketch diagram portraying the effects of vertical restriction by a mechanical layer (MTC) during fault growth and its predicted effect on fault geometrical data as a result of growth with preferential lengthening**.** Adapted from Soliva et al. (2005b).

**Figure 13:** Strike projections for the birfurcating faults (F6 and F7), displaying the geometry of, and throw distribution on, the fault surfaces with the Intra-Pliocene, Top Miocene, Top MTC and Top Eocene surfaces, respectively with depth. (a) F6: Maximum throw lies beneath the Top MTC surface and relay branchline (blue area). Overall, greater throw values encircle the relay zone which is associated with a throw minimum (white area). High throw gradients (*c.* 0.2) are present at the transition from the fault surface to the relay zone (sharp transition from blue to white area). (b) F7: Maximum throw lies coincident with the Top MTC surface on the main fault surface. Overall, greater throw values are present along strike at the structural level of the Top MTC surface.

**Figure 14:** Sketch diagrams of proposed growth histories for bifurcating faults. (a) F7: Individual precursor fault segments become vertically restricted by the regionally extensive MTC during downward propagation. As a result of this restriction precursor faults preferentially lengthen via segment linkage and the throw maxima migrate downwards as strain accumulation occurs at the restricted tip. Eventual strain accumulation overcomes the MTC restricting influence and continues downward propagation. (b) F6: Similarly to F7, an initial vertical restriction results in strain accumulation and throw maxima migration towards the MTC. Following overcoming the MTC's restricting influence, bifurcation at the MTC boundary occurs.

**Figure 15:** (a) A plot showing the relationship between the maximum throw on arcuate faults and their distance from the salt wall. In this fault group, the maximum throw observed on faults increases as the faults become more proximal to the salt wall. The deeper arcuate subgroup (A1-4) exhibit greater throws than the shallower (A5-9) subgroup. (b) A comparative plot of throw - length data between arcuate faults and that of other groups which exhibit similar maximum throw values. This plot highlights that, in comparison to other fault groups, arcuate faults are overdisplaced.

**Figure 16:** A variance co-blended depth structure map of the Intra-Pliocene surface (top right) showing the location of the seismic section showing the present-day structure of the salt minibasin (bottom right). The structure map also highlights the deeper part of the minibasin in the south and the onlap surface onto the salt wall. Hatched = presence of salt wall at this structural level. (a-d) A sketch diagram of the evolution of the minibasin in relation to the arcuate fault group. Evolution includes: a) sediment loading, b) salt withdrawal, diapirism, c-d) outer-arc bending and the subsequent onset of the nucleation of extensional arcuate faults. Data courtesy of CGG Multi-Client.

**Figure 1.**

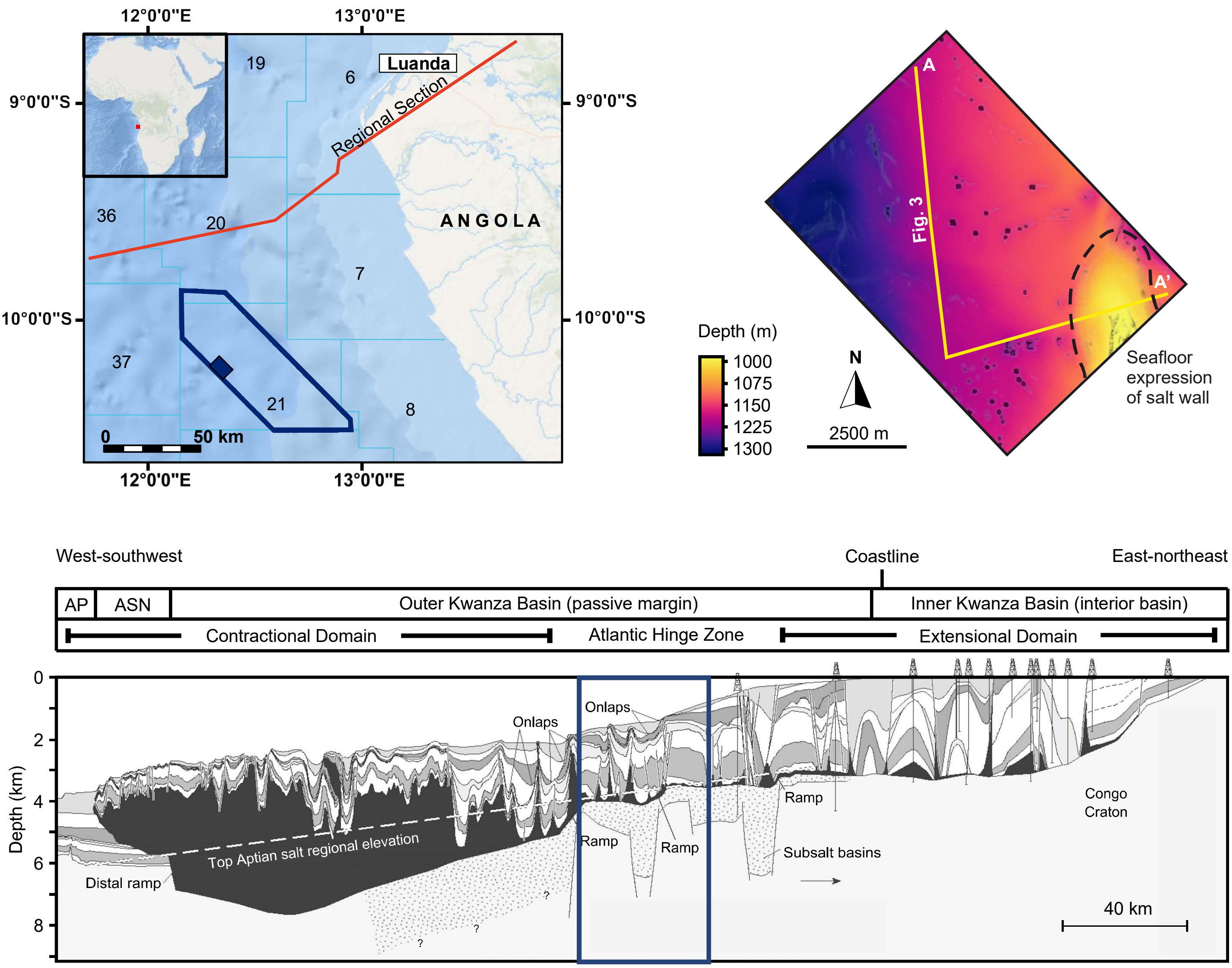
12°0'0"E
13°0'0"E
9°0'0"S
10°0'0"S
19
6
Luanda
Regional Section
36
20
ANGOLA
7
37
21
8
0
50 km
A
Fig. 3
A'
Depth (m)
1000
1075
1150
1225
1300
N
2500 m
Seafloor expression of salt wall
West-southwest
Coastline
East-northeast
AP
ASN
Outer Kwanza Basin (passive margin)
Inner Kwanza Basin (interior basin)
Contractional Domain
Atlantic Hinge Zone
Extensional Domain
Depth (km)
0
2
4
6
8
Onlaps
Onlaps
Ramp
Ramp
Ramp
Top Aptian salt regional elevation
Distal ramp
Subsalt basins
Congo Craton
40 km

**Figure 2.**

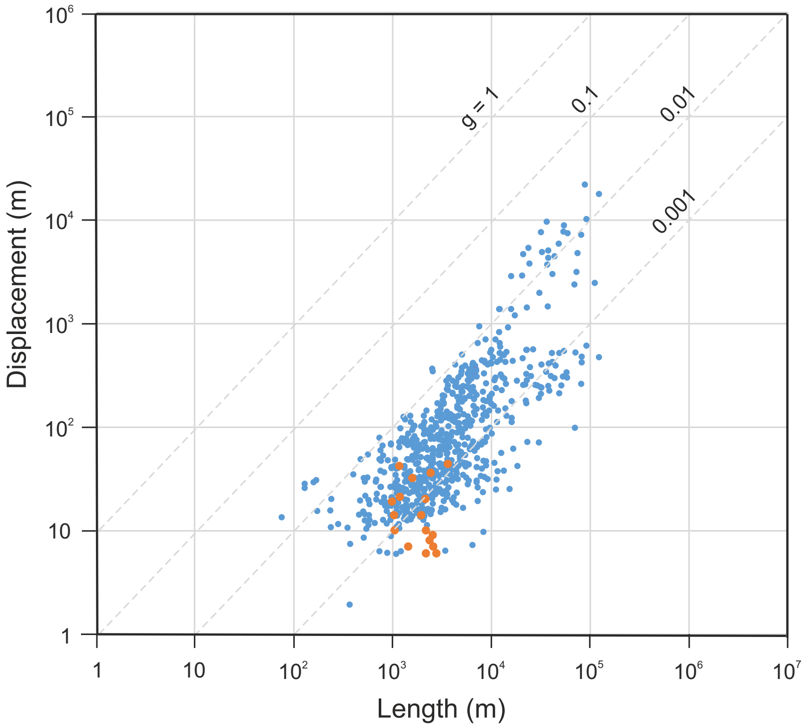

Displacement (m)
Length (m)
$10^6$
$10^5$
$10^4$
$10^3$
$10^2$
10
1
1
10
$10^2$
$10^3$
$10^4$
$10^5$
$10^6$
$10^7$
g = 1
0.1
0.01
0.001

**Figure 3.**

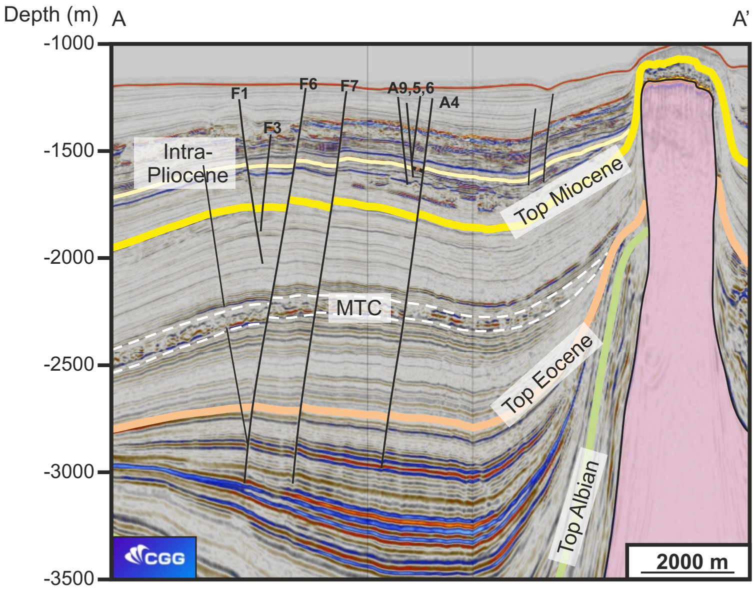

Depth (m)
A
A'
-1000
-1500
-2000
-2500
-3000
-3500
F1
F3
F6
F7
A9,5,6
A4
Intra-
Pliocene
Top Miocene
MTC
Top Eocene
Top Albian
CGG
2000 m

**Figure 4.**

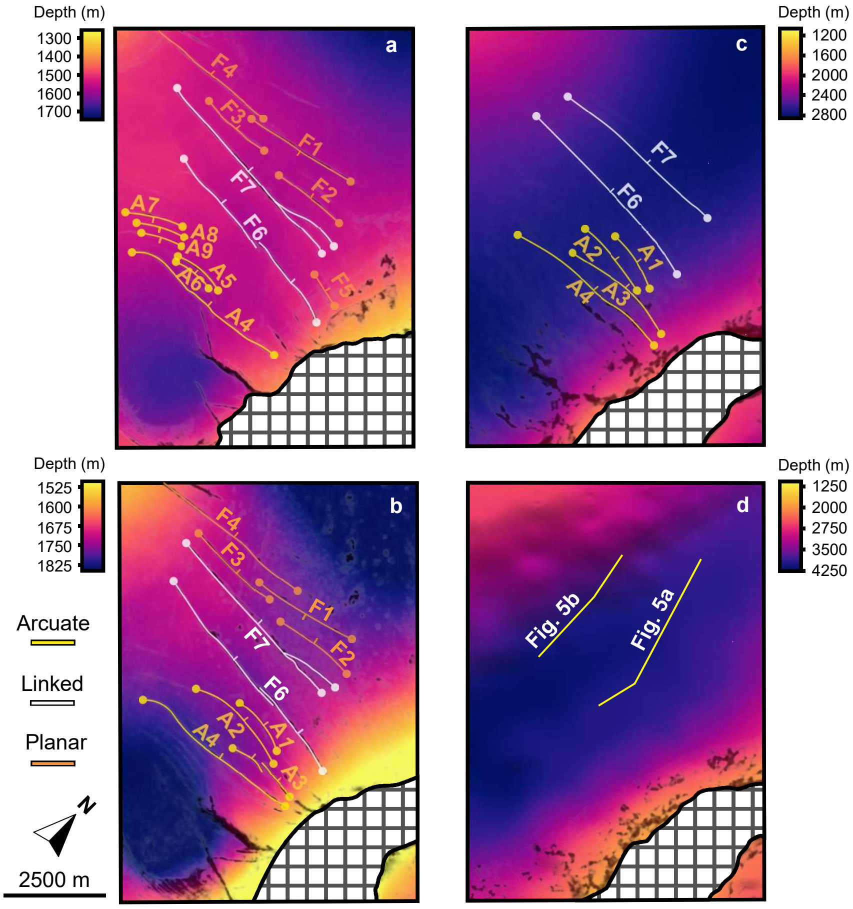

Depth (m)
1300
1400
1500
1600
1700
a
F4
F3
F1
F7
F2
A7
F6
A8
A9
A5
A6
F5
A4
c
Depth (m)
1200
1600
2000
2400
2800
F7
F6
A2
A1
A4
A3
Depth (m)
1525
1600
1675
1750
1825
b
F4
F3
F1
F7
F2
F6
A2
A1
A4
A3
Arcuate
Linked
Planar
N
2500 m
d
Depth (m)
1250
2000
2750
3500
4250
Fig. 5b
Fig. 5a

**Figure 5.**

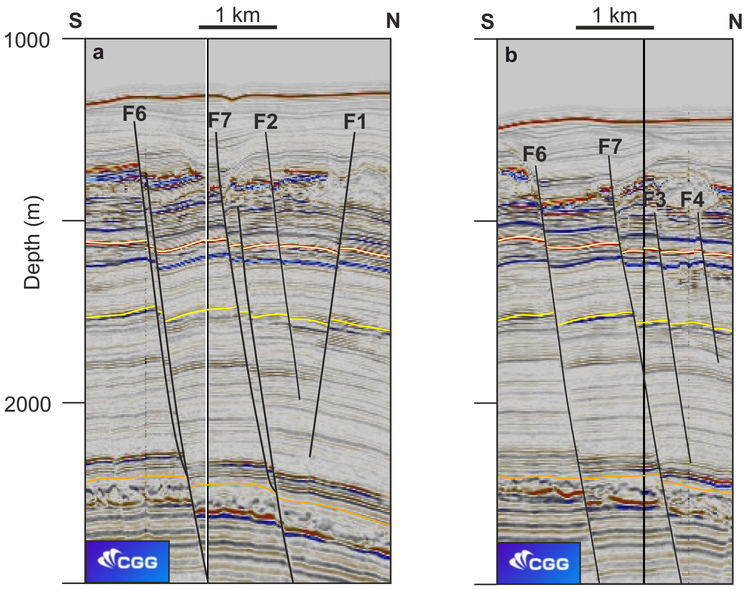
S
1 km
N
1000
2000
Depth (m)
a
F6
F7
F2
F1
CGG
S
1 km
N
b
F6
F7
F3
F4
CGG

**Figure 6.**

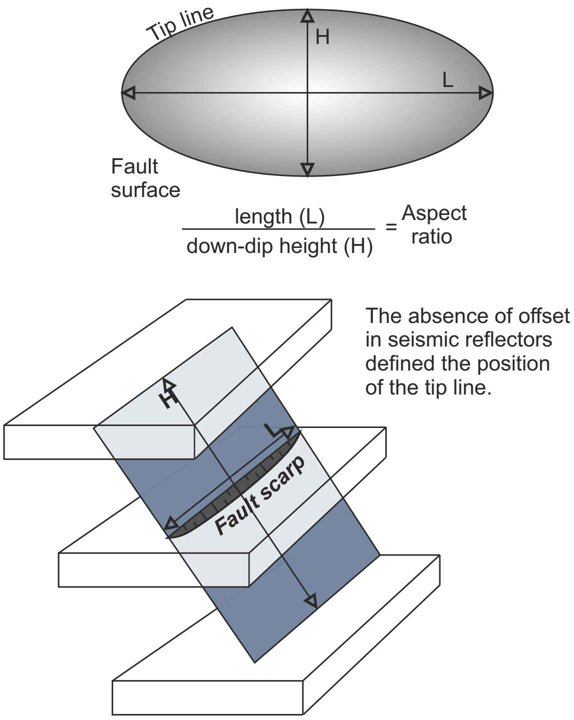
Tip line
H
L
Fault
surface
length (L)
down-dip height (H)
=
Aspect
ratio
The absence of offset
in seismic reflectors
defined the position
of the tip line.
H
L
Fault scarp

**Figure 7.**

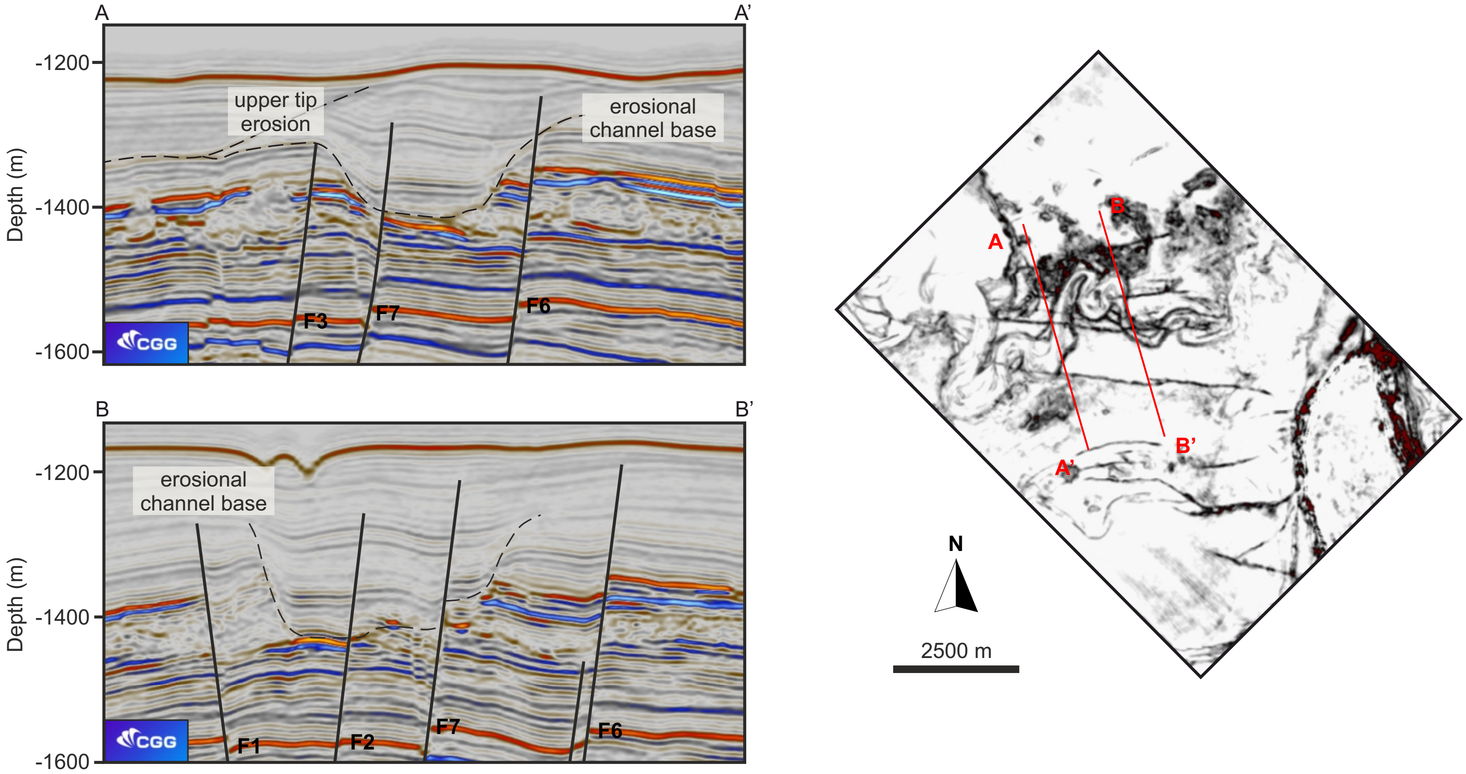
A
A'
-1200
-1400
-1600
Depth (m)
upper tip
erosion
erosional
channel base
F3
F7
F6
CGG
B
B'
erosional
channel base
F1
F2
F7
F6
A
B
A'
B'
N
2500 m

**Figure 8.**

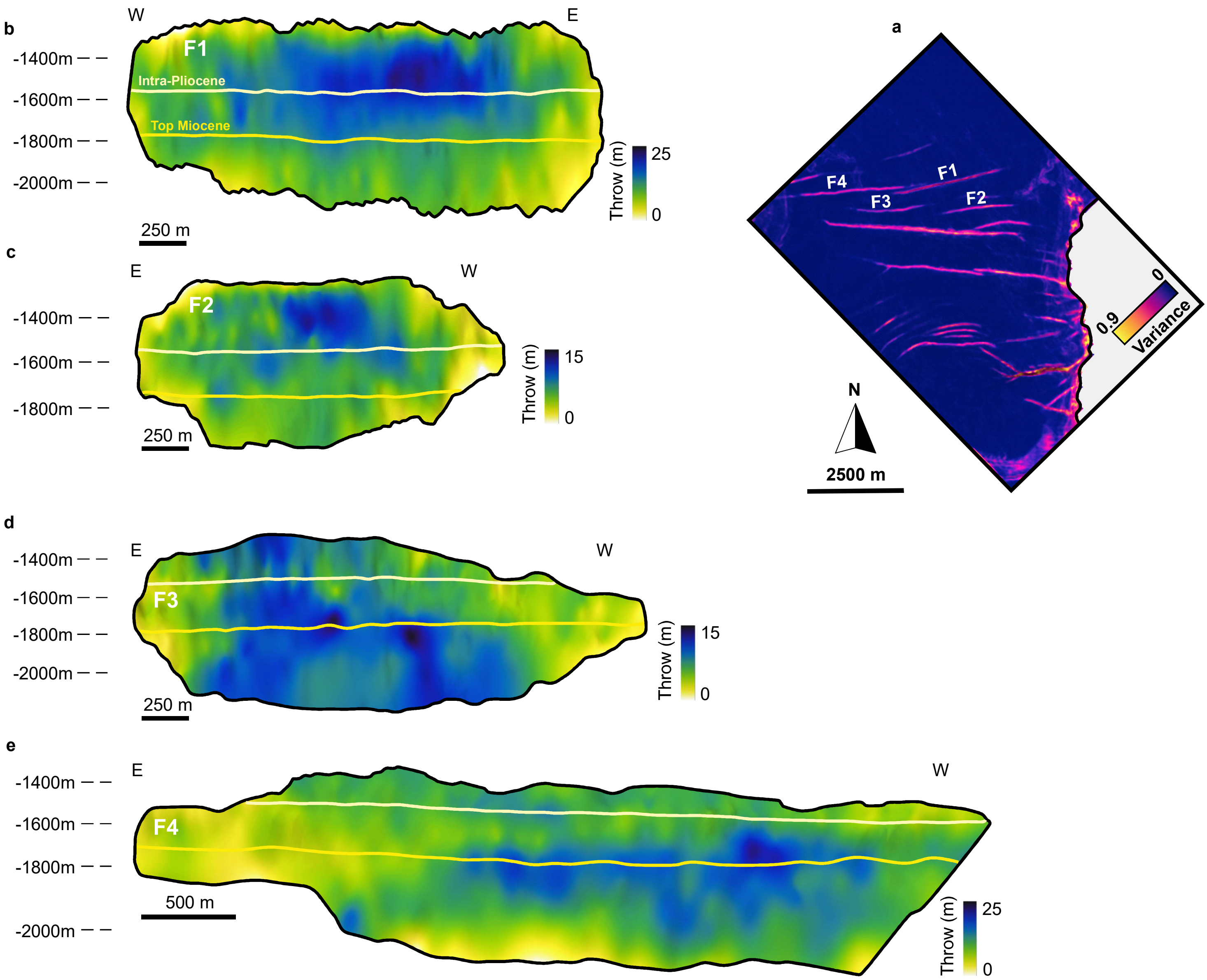

a
F4
F1
F3
F2
0
0.9
Variance
N
2500 m
b
W
E
F1
Intra-Pliocene
Top Miocene
-1400m
-1600m
-1800m
-2000m
Throw (m)
25
0
250 m
c
E
W
F2
-1400m
-1600m
-1800m
Throw (m)
15
0
250 m
d
E
W
F3
-1400m
-1600m
-1800m
-2000m
Throw (m)
15
0
250 m
e
E
W
F4
-1400m
-1600m
-1800m
-2000m
500 m
Throw (m)
25
0

**Figure 9.**

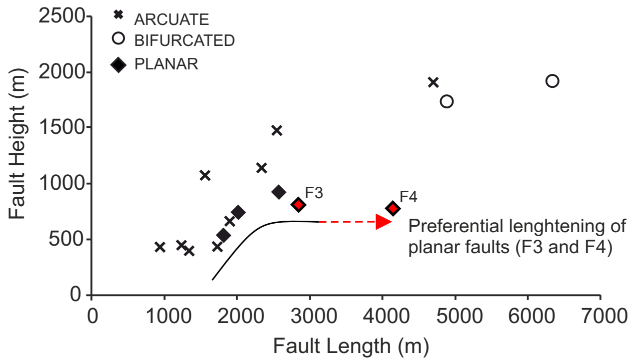
ARCUATE
BIFURCATED
PLANAR
Fault Height (m)
2500
2000
1500
1000
500
0
F3
F4
Preferential lenghtening of
planar faults (F3 and F4)
0
1000
2000
3000
4000
5000
6000
7000
Fault Length (m)

**Figure 10.**

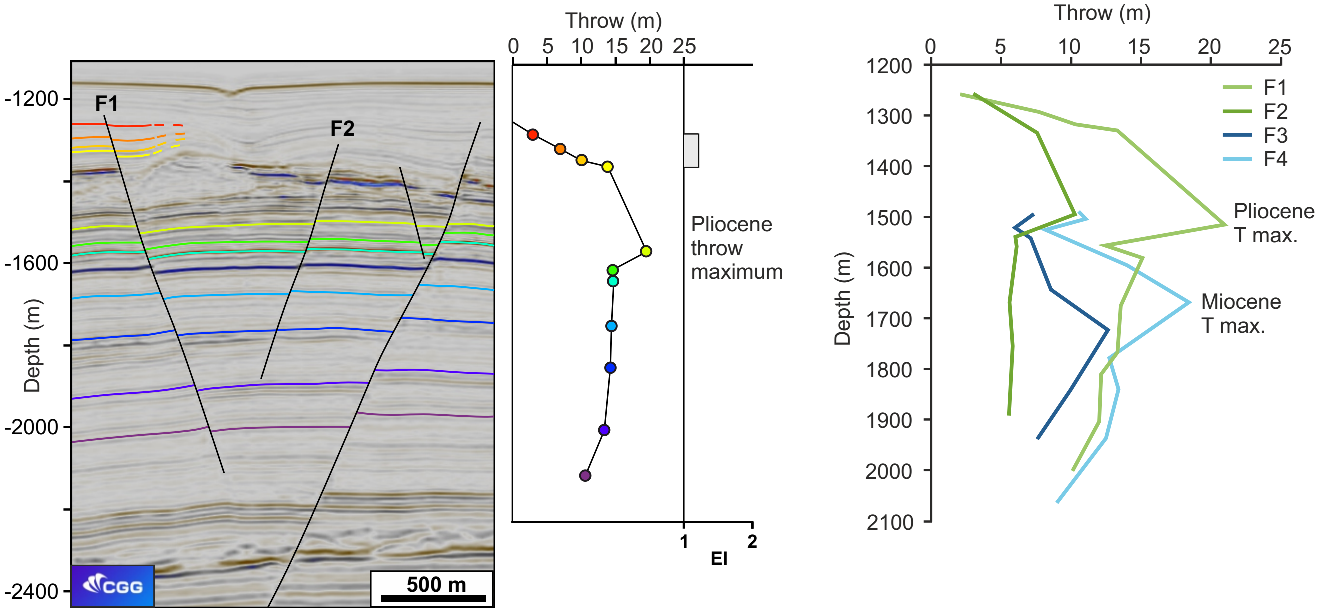

F1
F2
-1200
-1600
-2000
-2400
Depth (m)
CGG
500 m
Throw (m)
0 5 10 15 20 25
Pliocene throw maximum
1 2
EI
Throw (m)
0 5 10 15 20 25
1200 1300 1400 1500 1600 1700 1800 1900 2000 2100
Depth (m)
F1
F2
F3
F4
Pliocene T max.
Miocene T max.

**Figure 11.**

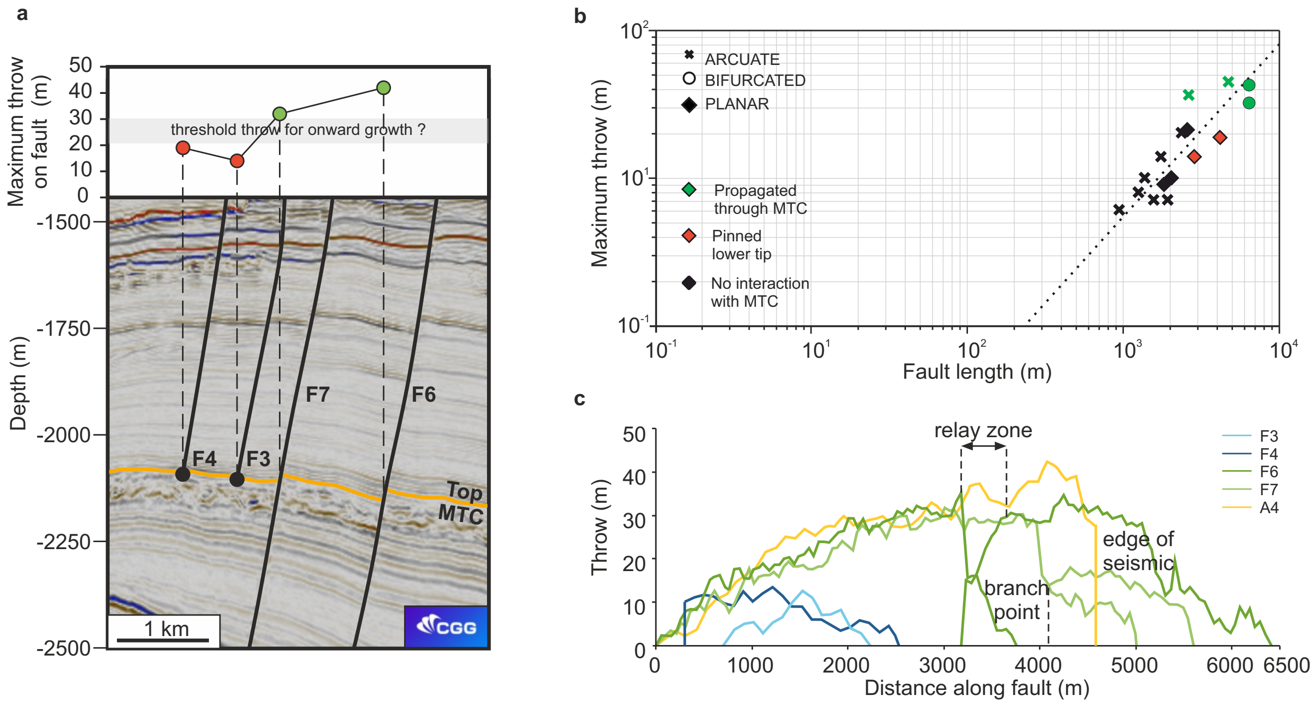
a
Maximum throw on fault (m)
50
40
30
20
10
0
threshold throw for onward growth ?
Depth (m)
-1500
-1750
-2000
-2250
-2500
F4
F3
F7
F6
Top MTC
1 km
CGG
b
Maximum throw (m)
ARCUATE
BIFURCATED
PLANAR
Propagated through MTC
Pinned lower tip
No interaction with MTC
Fault length (m)
c
Throw (m)
relay zone
branch point
edge of seismic
F3
F4
F6
F7
A4
Distance along fault (m)
0
1000
2000
3000
4000
5000
6000
6500

**Figure 12.**

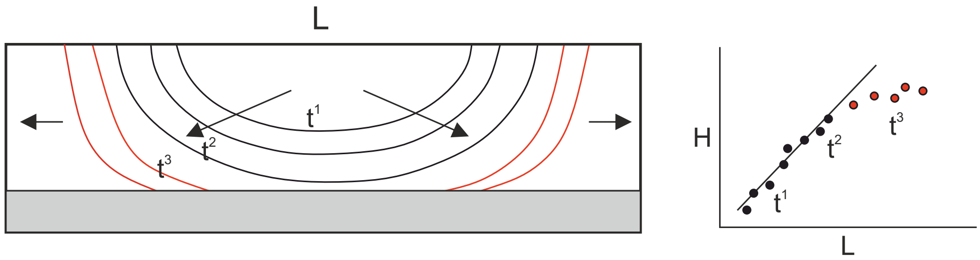

L
t1
t2
t3
H
t1
t2
t3
L

**Figure 13.**

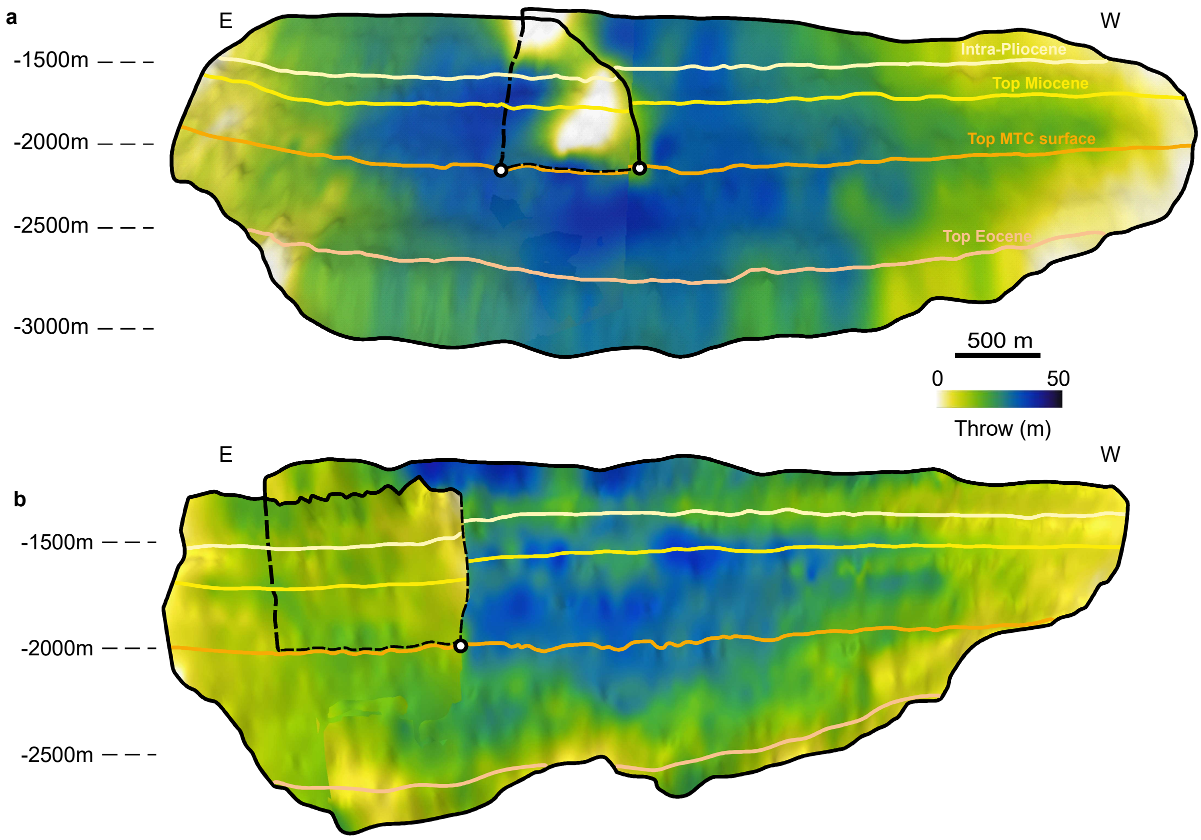
a
E
W
-1500m
-2000m
-2500m
-3000m
Intra-Pliocene
Top Miocene
Top MTC surface
Top Eocene
500 m
0
50
Throw (m)
b
E
W
-1500m
-2000m
-2500m

**Figure 14.**

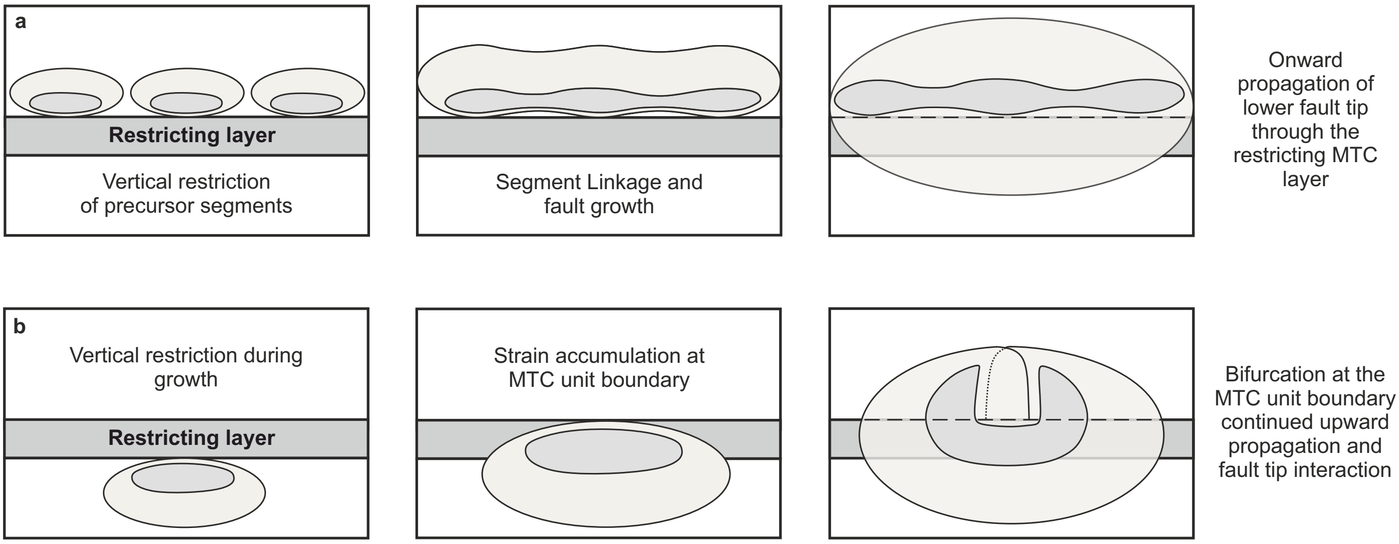
a
Restricting layer
Vertical restriction
of precursor segments
Segment Linkage and
fault growth
Onward
propagation of
lower fault tip
through the
restricting MTC
layer
b
Vertical restriction during
growth
Restricting layer
Strain accumulation at
MTC unit boundary
Bifurcation at the
MTC unit boundary
continued upward
propagation and
fault tip interaction

**Figure 15.**

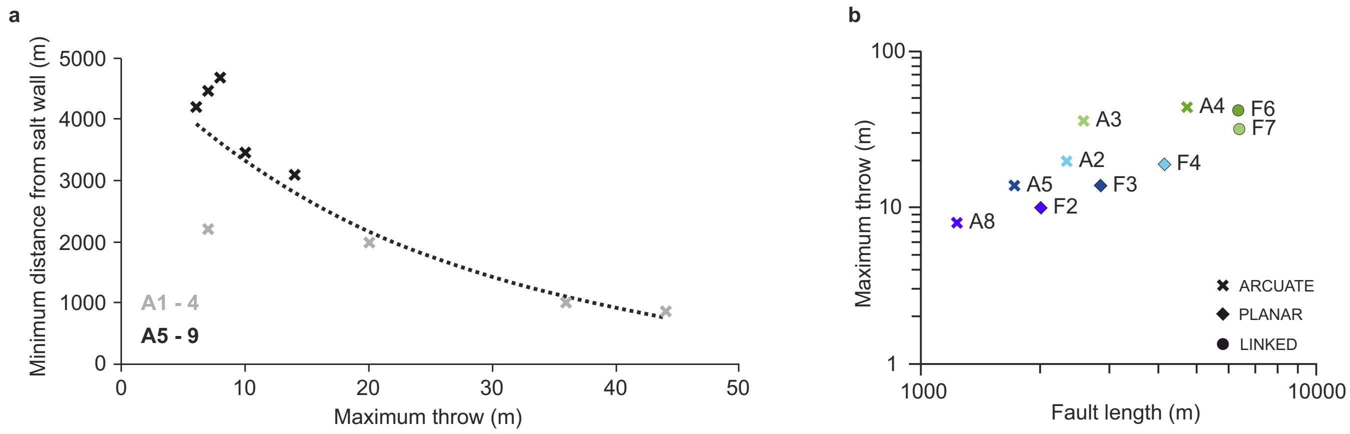

a
Minimum distance from salt wall (m)
5000
4000
3000
2000
1000
0
A1 - 4
A5 - 9
0
10
20
30
40
50
Maximum throw (m)
b
Maximum throw (m)
100
10
1
A3
A4
F6
F7
A2
F4
A5
F3
F2
A8
ARCUATE
PLANAR
LINKED
1000
10000
Fault length (m)

**Figure 16.**

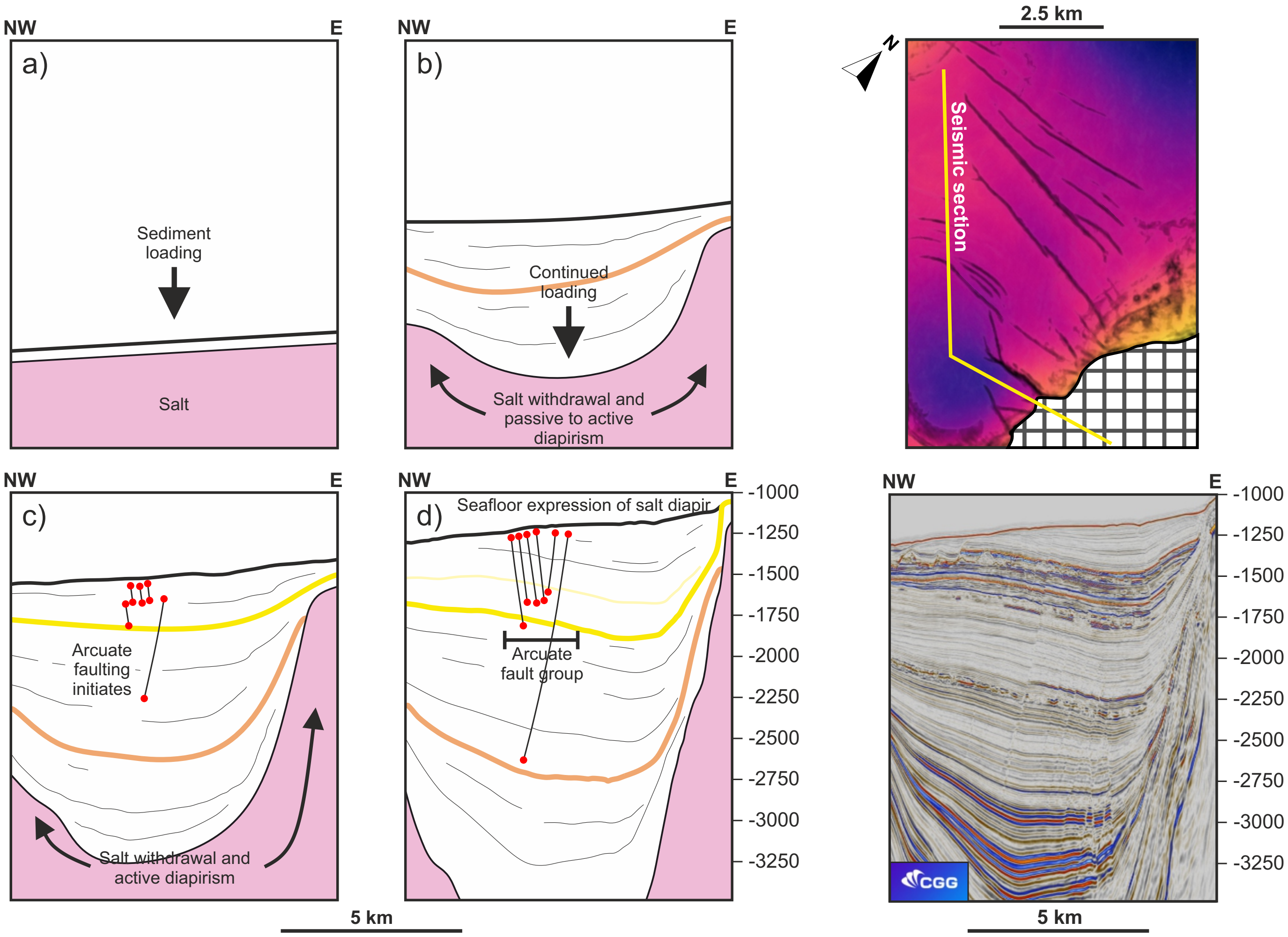

NW
E
a)
Sediment loading
Salt
b)
Continued loading
Salt withdrawal and passive to active diapirism
2.5 km
N
Seismic section
c)
Arcuate faulting initiates
Salt withdrawal and active diapirism
d)
Seafloor expression of salt diapir
Arcuate fault group
-1000
-1250
-1500
-1750
-2000
-2250
-2500
-2750
-3000
-3250
5 km
CGG